Renewable Energy 136 (2019) 968–992

Contents lists available at ScienceDirect

Renewable Energy

journal homepage: www.elsevier.com/locate/renene

Study of the flow fields over simplified topographies with different roughness conditions using large eddy simulations

Zhenqing Liu [a,*], Zheng Diao [a], Takeshi Ishihara [b]

[a] School of Civil Engineering & Mechanics, Huazhong University of Science and Technology, Wuhan, Hubei, China
[b] Department of Civil Engineering, School of Engineering, The University of Tokyo, Tokyo, Japan

ARTICLE INFO

Article history:
Received 10 August 2018
Received in revised form
25 December 2018
Accepted 10 January 2019
Available online 12 January 2019

Keywords:
LES
Topography
Turbulence flow fields
Vegetation canopy

ABSTRACT

The parameters influencing the wind turbine fatigue load calculations, such as two-point correlations R_{uu}, power spectrum density S_u, turbulent length scale L_u, skewness Sk_u, and kurtosis Ku_u of the wind are examined. Four simplified topographies, i.e., a 3D hill with smooth ground (3Ds), a 3D hill with rough ground (3Dr), a 2D ridge with smooth ground (2Ds), and a 2D ridge with rough ground (2Dr) are considered to investigate the influence from the shape of the topography and the ground roughness conditions. R_{uu} was found to vary considerably for different hill shapes and ground roughness conditions. Sk_u and Ku_u peaked in the shear layer region in the smooth cases, but not in the rough cases. S_u exhibited concentration in the wake in the 3Ds, 3Dr, and 2Ds cases, but not in the 2Dr case. In addition, a prominent increase in L_{ux} was observed just above the summit of the smooth 3D hill. The flow fields were further visualized using the enstrophy and Q-criteria. Coherent turbulent structures were observed to exist in the wake in the 3Ds, 3Dr, and 2Ds cases, whereas the flow was highly mixed in the wake in the 2Dr case.

1. Introduction

Most of the research about the wind over terrains in the field of wind energy is about the wind energy prediction [1–5]. However, the wind load is one of the controlling loads for the structural design of a wind turbine. The dynamic response of the wind turbines is very sensitive to the wind turbulence properties, such as the two-point correlations R_{uu}, power spectrum density S_u, and turbulent length scale Lu_u which are the key parameters required in the standard IEC61400–1 [6] for the generation of the turbulent wind fields using the analytical method during the wind turbine design process. Furthermore, skewness Sk_u and kurtosis Ku_u of the wind are the important parameter for deciding the shape of wind speed probability density function PDF which is important for the calculation of the wind turbines fatigue load [6–8]. Therefore, it is meaningful to carry out studies to examine the properties of the above mentioned parameters.

The wind properties over complex terrain have been studied by some researchers [9–14]. The investigated parameters are mainly the mean wind velocities, fluctuations, and the wind spectrum. The studies about the parameters, R_{uu}, Lu_u, Sk_u, and Ku_u are rare, which is the motivation of the present study. And in order to find the tendencies of the parameters as a functions of the terrain shape and the ground roughness conditions, we decide to choose simplified terrains, i.e., 3D hills and 2D ridges, to do this research.

The flow fields over 3D hills and 2D ridges have been studied extensively such as the examinations of the complexity of the topography [15,16], slope of the hills [17,18], surface roughness [19–23], and inflow conditions [24,25]. These investigations can also be divided into two groups: experimental studies [15–17,19,26–30] and numerical simulations [15,17,18,31–44]. In the following paragraphs, we will briefly review the achievements of the previous studies.

The models of isolated topographies examined in experiments are mainly 2D ridges [19,20,24,27,28] and 3D hills [26,29,45] with cosine-squared cross sections. Finnigan et al. [27] analyzed the flow field over a 2D ridge in physical streamline coordinates and found that in most flow regimes, the mean flow response was approximately inviscid. Ferreira et al. [17] studied the slope effects of 2D ridges on flow fields and found that the extension of the recirculating region was strongly dependent on the hill slope. The hill-top wind speed profiles as functions of surface roughness, hill shape, and hill slope were then investigated by Neff and Meroney [28],

* Corresponding author.
E-mail address: liuzhenqing@hust.edu.cn (Z. Liu).

https://doi.org/10.1016/j.renene.2019.01.032
0960-1481/

Nomenclature

$C_{D,\tilde{u}_i}$	drag coefficient
C_s	Smagorinsky constant
d	distance from cell center to the closest wall [m]
E_{avg}	time averaged enstrophy [s $^{-2}$]
h	height of the topographies [m]
f	non-dimensional frequency
$f_{\tilde{u},i}$	source term in momentum equation
h'	second vertical coordinate [m]
h_t	height of vegetation [m]
h_w	wake depth [m]
Kuu_i	kurtosis of u_i
L	length in the streamwise direction of the topographies [m]
L_i	fine grid domain extensions in x, y and z directions [m]
Lu_{xi}	turbulence length scale [m]
L_s	mixing length for subgrid-scales [m]
n	natural frequency [Hz]
P	mean pressure [N m^{-2}]
p	rms of fluctuating pressure [N m^{-2}]
$\tilde{p}$	filtered pressure [N m^{-2}]
Q	value of the Q-criteria [s $^{-2}$]
Re	Reynolds number
R_u	self-correlation function
$R_{u_iu_i}$	zero time-lag two-point correlation coefficients
$\tilde{S}_{ij}$	rate-of-strain tensor for the resolved scale [s $^{-1}$]
Sku_i	skewness of u_i
S_u	PSD of streamwise velocity
t	time [s]
U, V, W	mean streamwise, spanwise, and vertical velocities [m s^{-1}]
u, v, w	rms of fluctuating streamwise, spanwise, and vertical velocities [m s^{-1}]
U_{down}	mean streamwise velocity downstream of the topographies [m s^{-1}]
U_e	mean streamwise velocity in experiments [m s^{-1}]
u_e	velocity fluctuations in experiments [m s^{-1}]
U_h	mean streamwise velocity upstream of the topographies at h [m s^{-1}]
U_{up}	mean streamwise velocity upstream of the topographies [m s^{-1}]
$\tilde{u}_i$	filtered velocities [m s^{-1}]
u_τ	friction velocity [m s^{-1}]
x, y, z	Cartesian coordinates [m]
x_{iref}	coordinates of the reference points [m]
z_s	shape of the topographies [m]

Greek

Δ	volume of a computational cell [m^3]
Δt	time step size [s]
Δt^*	time step size in convective units
Δx_i	grid size [m]
δ_{ij}	Kronecker delta
κ	von Kármán constant
μ	air viscosity [Pa·s]
μ_t	SGS turbulent viscosity [Pa·s]
ω_i	vorticity component of the flow along x_i [s $^{-1}$]
Ω_{ij}	symmetric components of the velocity-gradient tensor [s $^{-2}$]
ρ	air density [kg m^{-3}]
τ	time lag [s]
τ_{ij}	SGS stress [N m^{-2}]

Abbreviations

2D	two dimensional
2Dr	2D ridge with rough ground
2Ds	2D ridge with smooth ground
3D	three dimensional
3Dr	3D hill with rough ground
3Ds	3D hill with smooth ground
CFD	Computational Fluids Dynamics
CFL	Courant Friedrichs Lewy
FVM	Finite Volume Method
IPM	Isotropization of Production Model
LES	Large Eddy Simulations
N-S	Navier-Stokes
PDF	Probability Density Function
PSD	Power Spectrum Density
RANS	Reynolds Averaged Navier-Stokes
rms	root mean square
RNG	*Re*-Normalization Group
SIMPLE	Semi-Implicit Pressure Linked Equations
SGS	subgrid scale

whose experimental results suggested that the wind speeds near the ground increased substantially when there was no roughness at the crest. The effects of roughness, including sudden changes in the roughness conditions, were subsequently studied in detail by Takahashi et al. [19] and Cao and Tamura [20,30]. The roughness both on the hill surface and on the upstream ground was found to affect the speed-up ratio over the hill. The separation bubble of a rough hill extended further downstream, resulting in a reattachment length greater than that of a smooth hill. Finally, the effects of local wind direction on speed-up over a 2D ridge was examined by Lubitz and White [24], who observed that the speed-up could vary significantly depending on the approaching wind direction.

Because the flow fields over 3D hills are much more complex than those over 2D ridges, only a few experimental studies have been conducted using such topography. Gong and Ibbetson [26] measured the flow over a 3D hill and a 2D ridge. The results suggested that the mean flow and turbulence were broadly similar but that the perturbation amplitude for the 3D hill was reduced. Ishihara et al. [29] investigated the flow field over a 3D hill by using split-fiber probes designed for measuring flows with high turbulence and separation. Pronounced speed-up of the flow was observed at the summit and the upwind midway. Takahashi et al. [45] examined the effects of atmospheric stability on the flow field of the boundary layer over a 3D hill. The wind velocity was measured by using a 3D laser Doppler anemometer. Owing to the instability of the flow, the turbulent velocity was less than that in stable conditions.

However, the 3D views of the flow fields over hills are limited. Furthermore, there have been few studies on the space correlations and length scale of the wind velocity over 3D hills and 2D ridges. Considering their ability to obtain the full information of flow fields, computational fluid dynamics methods have been widely adopted to model the flow over various topographies and can be divided into two main types of approaches: Reynolds-averaged

Navier–Stokes (RANS) methods and large eddy simulations (LESs).

For RANS methods, two-equation models have been widely applied, among which the performances of the following models have been examined: an isotropic eddy-viscosity k-ε extension model [31], a modified low-Reynolds number k-ε model [17], a standard k-ε model [15,32–34,37–39,44], an isotropization of production model [46], Shih and Durbin models [47], a renormalization group k-ε model [37], and k–ω models [37,44]. However, the numerical results of the RANS methods have revealed that they cannot predict the flow fields in wakes very well. Furthermore, the space correlations of the wind velocities in instantaneous flow fields cannot be obtained.

LESs can provide more detailed information in space and time. Iizuka and Kondo [35] examined several subgrid scale (SGS) models (i.e., the standard Smagorinsky, dynamic Smagorinsky, Lagrangian dynamic Smagorinsky, and hybrid SGS models) considering the ground roughness conditions. Iizuka and Kondo [36] then studied the performance of three additional modified SGS models, and the best one (denoted as I0 in their study, which models the SGS Reynolds stress by using the scale-similarity concept) was proposed. The LESs investigated by Tamura et al. [48,49] showed high accuracy for hills with moderate slopes. For a steep hill, there was a clear discrepancy between the LES and experimental turbulence statistics in the separated region. Wan and Agel [40] studied the performances of three SGS models (i.e., the standard Smagorinsky, Lagrangian dynamic Smagorinsky, and scale-dependent Lagrangian dynamic models), where the last one produced more realistic turbulence statistics, as was also observed by Ma and Liu [43]. In that study, it was also found that a higher horizontal grid resolution could improve the results behind an escarpment, while a higher vertical grid resolution could improve the results on the lee side of a hill. Cao et al. [18] and Liu et al. [25,42] adopted the Smagorinsky-Lilly SGS model to the flow over terrain with different roughness conditions. The LES results agreed well with the experimental results, confirming the ability to predict flow over topographies using LESs. Liu et al. [50] examined the coherent flow structures over an isolated smooth 3D hill and provided the explanations of the double peaks on the profiles of the fluctuations of the spanwise velocity, however there is no discussion about the velocity spectra and the turbulence length scale which are two important parameters when generating the wind using Weighted Amplitude Wave Superposition (WAWS) method. The previously conducted LESs of flow over simplified topographies are summarized in Table 1.

However, skewness Sk_u and kurtosis Ku_u, which are two important parameters relating to the estimation of the probability density function (PDF) of wind velocity, have rarely been studied for the simplified topographies, i.e., 3D hill and 2D ridge with different roughness conditions. In addition, few studies have been conducted on wind velocity spectra as well as the turbulence length scale over 3D hills and 2D ridges. Furthermore, in China the construction of wind farm is now moving to the central and the eastern part of China where the terrain is always covered by vegetation which will make the surface of the terrain much rougher than those in the northern part of China where most of the wind farms in China were constructed in the past 10 years. Therefore, clarification of the difference of the key parameters relating with the calculation of the wind loads on the wind turbines for the smooth and rough topographies will be an important issue. Fig. 1 shows the typical simple topographies. The smooth 3D hill and smooth 2D ridge in Fig. 1 locates in Xinjiang Province (northern part of China), and the rough 3D hill as well as the rough 2D ridge in Fig. 3 locates in Anhui Province (Eastern part of China).

In the present study, LESs were performed to reproduce the turbulent flow fields observed over simplified topographies. Four cases were examined: a 3D hill with smooth ground (3Ds), a 3D hill with rough ground (3Dr), a 2D ridge with smooth ground (2Ds), and a 2D ridge with rough ground (2Dr). The simulation is in experimental scale. The decision of choosing the experimental scale instead of the full scale is from the consideration that the full experimental data is available and it has been found by Kasmi and Masson [11] that the properties are similar between the wind tunnel scale and the full scale flow fields over terrains. This paper introduces the details of the model, including the numerical methods and configuration of the numerical wind tunnel, and discusses the two-point correlations R_{uu}, Sk_u, Ku_u, S_u, and Lu_x of the streamwise velocity. The flow fields are further described by using the enstrophy E and Q-criteria Q.

2. Numerical models

In section 2.1, we introduce the governing equations and structures of the numerical models. The computational domain, grid system, and boundary conditions are presented in sections 2.2–2.4. The solution schemes are described in section 2.5. Finally, the grid independence is discussed in section 2.6.

2.1. Governing equations

LES lies between RANS method and DNS (Direct Numerical Simulation) method. It is motivated by each of the limitations of RANS and DNS approaches. Because the large-scale unsteady motions are represented explicitly, LES can be expected to be more accurate and reliable than RANS method for flows in which large-scale unsteadiness is significant —— such as the flow over topographies. Besides, eddies smaller than the cell sizes are modeled by SGS models, and therefore the node number could be less than that

Table 1
Previous LES about the simplified terrains.

Authors	Time	Terrain shape	Ground condition	Mean velocities	Fluctuations	Correlation	Skewness &Kurtosis	Spectrum	Turbulence Length scale
Izuka and Kondo	2004	2D ridge	Smooth and Rough	●	●	○	○	○	○
Izuka and Kondo	2006	2D ridge	Smooth and Rough	●	●	○	○	○	○
Tamura et al.	2007	2D ridge	Smooth and Rough	●	●	○	○	●	○
Tamura et al.	2007	3D hill	Smooth and Rough	●	●	○	○	○	○
Wan and Agel	2011	2D ridge	Rough	●	●	○	○	○	○
Cao et al.	2012	2D ridge	Smooth and Rough	●	●	○	○	○	○
Liu et al.	2016	2D ridge and 3D hill	Smooth	●	●	○	○	●	○
Liu et al.	2016	3D hill	Rough	●	●	○	○	○	○
Ma and Liu	2017	3D hill	Rough	●	●	○	○	○	○
Liu et al.	2018	3D hill	Smooth	●	●	●	●	○	○
Present	2018	2D ridge and 3D hill	Smooth and Rough	●	●	●	●	●	●

● means yes, ○ means no.

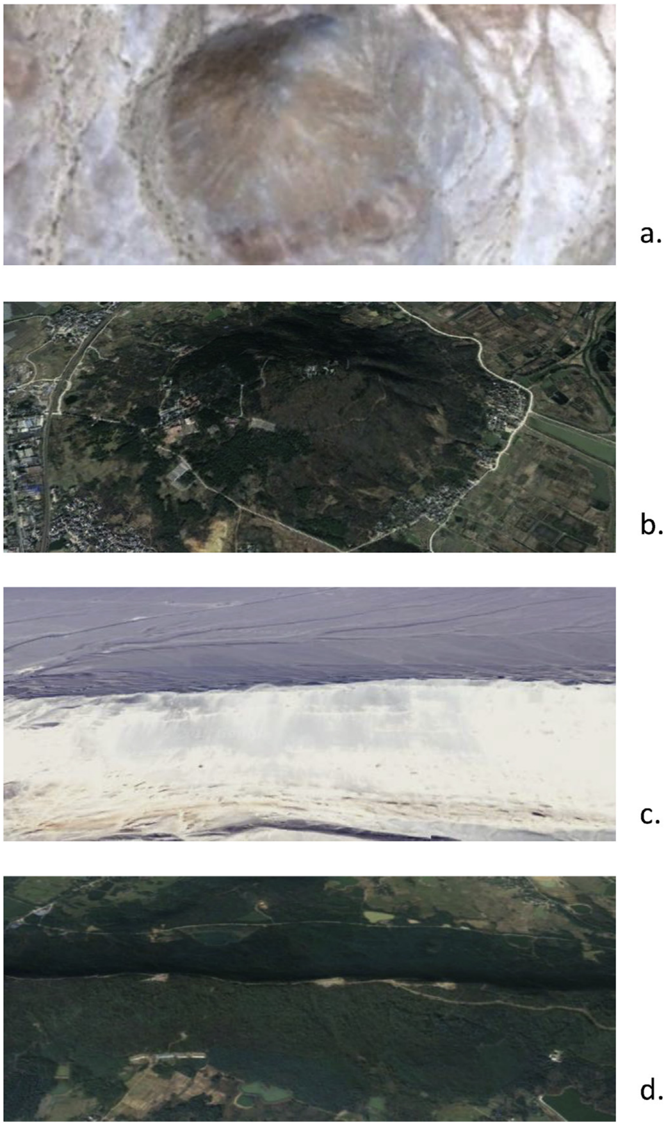

Fig. 1. Typical topographies, (a) smooth 3D hill, (b) rough 3D hill, (c) smooth 2D ridge, and (d) rough 2D ridge.

in DNS. In the last decade, with the development of the capability of computer systems, the applications of large eddy simulations for the study of the flow over topographies have increased. Therefore, in the present study, LES turbulence model is applied, in which the Boussinesq hypothesis is employed and the standard Smagorinsky-Lilly model [51,52] is adopted. By filtering the time-dependent Navier-Stokes (N-S) equation in Cartesian coordinates x_i (x, y, z), the governing equations are obtained:

$$\frac{\partial \rho \tilde{u}_i}{\partial x_i} = 0 \tag{1}$$

$$\frac{\partial \rho \tilde{u}_i}{\partial t} + \frac{\partial \rho \tilde{u}_i \tilde{u}_j}{\partial x_j} = \frac{\partial}{\partial x_j}\left(\mu \frac{\partial \tilde{u}_i}{\partial x_j}\right) - \frac{\partial \tilde{p}}{\partial x_i} - \frac{\partial \tau_{ij}}{\partial x_j} \tag{2}$$

where ρ is the density; $\tilde{u}_i$ and $\tilde{p}$ are the filtered velocities and pressure, respectively; t is time; μ is the viscosity; τ_{ij} is the SGS stress. In order to close the equations for the filtered velocities, a model for the anisotropic residual stress tensor τ_{ij} is needed, which is modeled as follows:

$$\tau_{ij} = -2\mu_t \tilde{S}_{ij} + \frac{1}{3}\tau_{kk}\delta_{ij} \tag{3}$$

$$\tilde{S}_{ij} = \frac{1}{2}\left(\frac{\partial \tilde{u}_i}{\partial x_j} + \frac{\partial \tilde{u}_j}{\partial x_i}\right) \tag{4}$$

where μ_t denotes the SGS turbulent viscosity, $\tilde{S}_{ij}$ is the rate-of-strain tensor for the resolved scale, and δ_{ij} is the Kronecker delta. The Smagorinsky-Lilly model is used for the SGS turbulent viscosity [53]:

$$\mu_t = \rho L_s^2 \left|\tilde{S}\right| = \rho L_s^2 \sqrt{2\tilde{S}_{ij}\tilde{S}_{ij}} \tag{5}$$

$$L_s = min\left(\kappa d,\ C_s \Delta^{1/3}\right) \tag{6}$$

in which L_s denotes the mixing length for subgrid-scales, κ is the von Kármán constant, i.e., 0.42, d is the distance to the closest wall and Δ is the volume of a computational cell. In this study, C_s is the Smagorinsky constant, which is determined to be 0.1 same as the study by Iizuka and Kondo [36].

When the cells are in the laminar sublayer, the shear stresses are obtained from the laminar stress-strain relation

$$\frac{\tilde{u}}{u_\tau} = \frac{\rho u_\tau y}{\mu} \tag{7}$$

If the mesh cannot resolve the laminar sublayer, it is assumed that the centroids of the cells fall within the logarithmic region of the boundary layer, and the law-of-the-wall is employed as

$$\frac{\tilde{u}}{u_\tau} = \frac{1}{\kappa} lnE\left(\frac{\rho u_\tau y}{\mu}\right) \tag{8}$$

where y is the distance between the center of the cell and the wall, u_τ is the friction velocity, and the constant E is 9.793.

Canopy model has been applied to simulate the roughness canopy in some studies [25,54], in which an appropriate source term, $f_{\tilde{u},i}$, is added in momentum equation:

$$\frac{\partial \rho \tilde{u}_i}{\partial t} + \frac{\partial \rho \tilde{u}_i \tilde{u}_j}{\partial x_j} = \frac{\partial}{\partial x_j}\left(\mu \frac{\partial \tilde{u}_i}{\partial x_j}\right) - \frac{\partial \tilde{p}}{\partial x_i} - \frac{\partial \tau_{ij}}{\partial x_j} + f_{\tilde{u},i} \tag{9}$$

$$f_{\tilde{u},i} = -\rho C_{D,\tilde{u}_i} \frac{\gamma_0}{l_0} \tilde{u}_{mag} \tilde{u}_i \tag{10}$$

where, $C_{D,\tilde{u}_i}$ is the drag coefficient, γ_0 is the volume occupancy rate; l_0 is the thickness of the leaf. $C_{D,\tilde{u}_i} = 0.4$ has been adopted in the studies by Liu et al. [42] and the boundary layer flow with rough ground condition has been successfully reproduced. The height of vegetation, h_t, is 5 mm and covers the entire ground of the computational domain.

For roughness blocks, due to the fact that the volume of the single block is much larger than that of the grid, the grid occupied by the blocks should represent the solid body. As a result, $C_{D,\tilde{u}_i}\frac{\gamma_0}{l_0} = 1.0 \times 10^4$ is applied here. It is not necessary to explicitly build the geometry of the blocks. If the grid cells are located in the roughness blocks, the drag force terms given in Eqs. (9) and (10) will be added in the momentum equation to represent the effects of the solid blocks. If the arrangement of the roughness blocks is changed, it is not necessary to rebuild the model. In this circumstance, the function determining the geometries of the blocks only requires modification.

2.2. Computational domain

The simulation in wind tunnel scale is adopted. It is from the considerations that the full experimental data is available and it has been found by Kasmi and Masson [11] that the wind properties are similar between the wind tunnel scale and the full scale flow fields over terrains. Experimental data obtained from the report by Ishihara et al. [29] were used to evaluate the performance of the numerical wind tunnel. In that experiment, a return wind tunnel with a test section 1.1 m wide, 0.9 m high, and 7 m long was employed. Cubic elements with heights of 60 mm, 20 mm, and 10 mm covered 1.2 m of the floor at the inlet of the test section. Each group of blocks consisted of three rows, and the roughness blocks covered a 0.4 m long region in the streamwise direction. The areal densities of the blocks with heights of 60 mm, 20 mm, and 10 mm were 25%, 2.8%, and 0.7%, respectively. The origin was located at 3.4 m downstream from the roughness blocks.

To reproduce the experimental data, the configuration of the numerical wind tunnel was designed to be the same as that in the experiment, except for the widths of the wind tunnel and the upstream necking zone (see Fig. 2(a)). The detailed arrangement of the roughness blocks is depicted in Fig. 2(b). Mason and Thomson [55] recommended a width of approximately two times the boundary layer depth to reproduce the largest eddies in the atmospheric boundary layer. Considering the convenience of roughness block generation, 1.8 times the boundary layer thickness, i.e., 0.66 m, was selected for the width. The 2.0 m long upstream buffer zone was appended to avoid any perturbations in the turbulence generation region due to the inlet conditions. The outlet of the numerical wind tunnel was set 2.4 m from the origin, which was 60 times the height of the simulated 3D hill, to avoid any influence from the outlet on the concerned region.

The same 3D hill shape that was used in the experimental study by Ishihara et al. [29], $z_s(x,\ y)\ =\ hcos^2\pi(x^2+y^2)^{1/2}/2L$, as well as the same 2D ridge shape, $z_s(x,\ y)\ =\ hcos^2\pi x/2L$, were adopted,

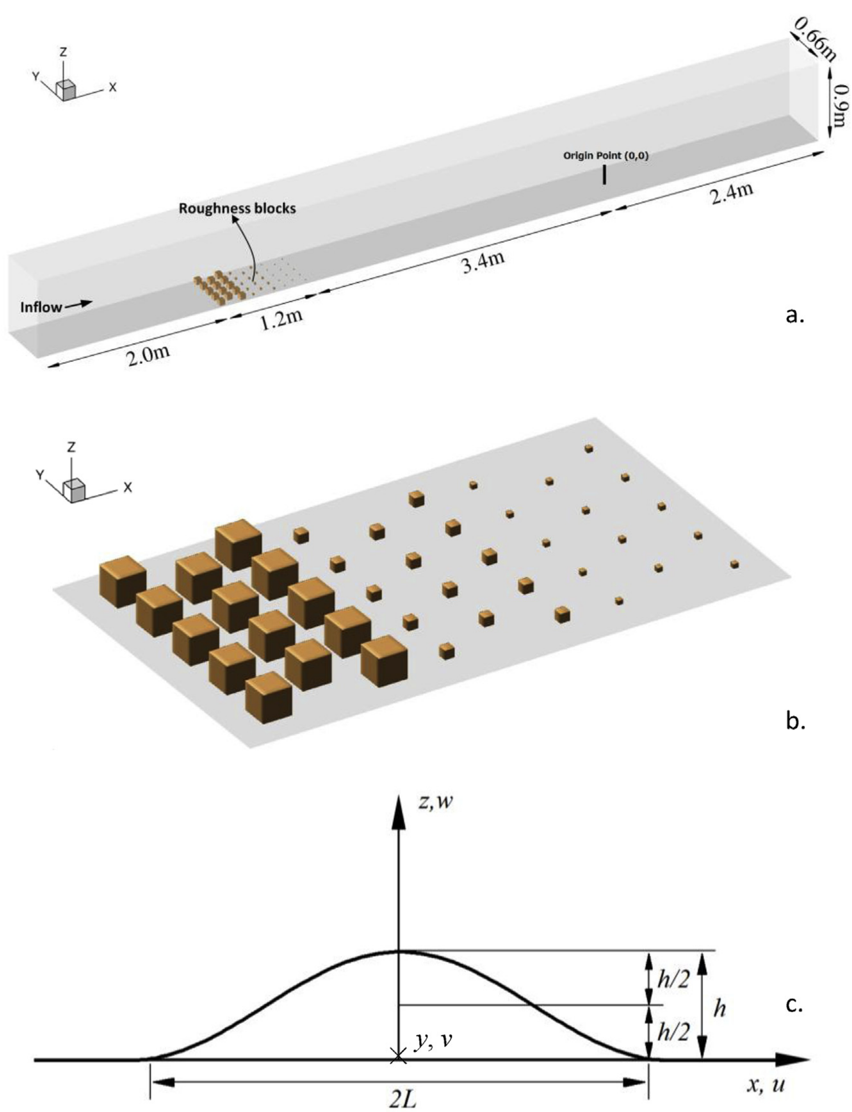

Fig. 2. Numerical model. (a) geometry of the numerical wind tunnel. Brown area shows the region occupied by the roughness blocks, (b) details of the arrangement of the roughness blocks, (c) coordinates and notations used in this study. (For interpretation of the references to color in this figure legend, the reader is referred to the Web version of this article.)

where $h = 40$ mm is the height of the 3D hill or 2D ridge and $L = 100$ mm is the length in the streamwise direction of the 3D hill or 2D ridge. The maximum slope was about 32°. Fig. 2(c) shows a side view of the 3D hill together with the coordinate system used in this study, where x, y, and z are the streamwise, spanwise, and vertical directions, respectively. In the x-direction, the zero-point is the center of the topography. A second vertical coordinate, $h' = z - z_s(x, y)$, was used to denote the height above the local surface. The 3D views of the four topographies are provided in Fig. 3.

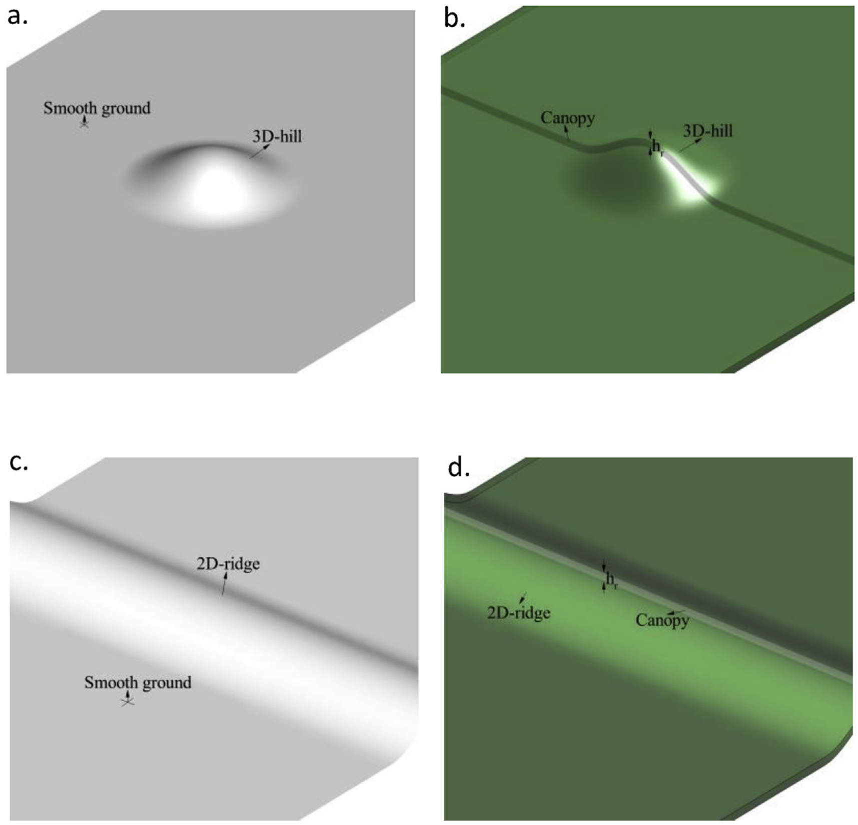

Fig. 3. Three dimensional view of four topographies. (a) smooth 3D hill, (b) rough 3D hill, (c) smooth 2D ridge, and (d) rough 2D ridge. The crosswind cross section of the vegetation canopy is drown by gray color. (For interpretation of the references to color in this figure legend, the reader is referred to the Web version of this article.)

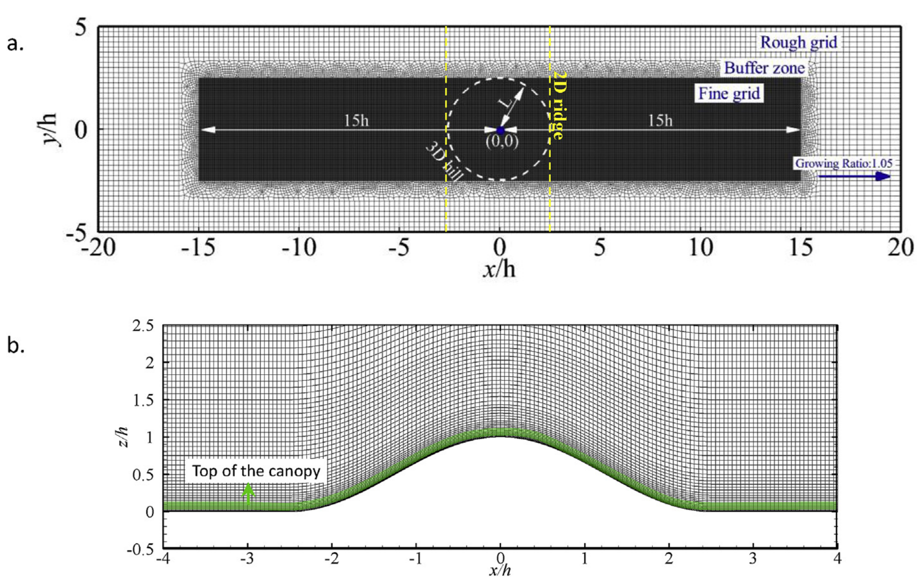

Fig. 4. Mesh of the numerical model. (a) Sketch map of the locations of the rough grid, buffer zone, and fine grid of the nested grid. White dashed line circles the region covered by a 3D hill. Yellow dashed lines show the region of 2D ridges. x and y axis have been normalized by h. (b) distributions of the mesh on the vertical slice crossing the center of the 3D hill. x and z axis have been normalized by h. The vegetation canopy is colored by green. (For interpretation of the references to color in this figure legend, the reader is referred to the Web version of this article.)

Table 2
Settings for the boundary conditions.

Locations	Boundary type	Expression
Outlet	Pressure outlet	$\partial\tilde{p}/\partial n = 0$, $\partial\tilde{u}_i/\partial n = 0$
Top	Symmetry	$\partial\tilde{u}/\partial n = 0$, $\partial\tilde{v}/\partial n = 0$, $\tilde{w} = 0$
spanwise Sides	Symmetry	$\partial\tilde{u}/\partial n = 0$, $\partial\tilde{w}/\partial n = 0$, $\tilde{v} = 0$
Inlet	Velocity inlet	$\partial\tilde{p}/\partial n = 0$, $\tilde{u} = 5.4\ \mathrm{m\,s^{-1}}$, $\tilde{v} = 0$, $\tilde{w} = 0$
Ground	Non-slip wall	$\partial\tilde{p}/\partial n = 0$, $\tilde{u}_i = 0$

2.3. Grid system

To limit the impacts of the symmetric boundary conditions and to simulate the flow over the isolated 3D hills and 2D ridges with an acceptable computational time, the grid nesting procedure was adopted, as presented in Fig. 4. The dark gray area represents the fine grid region, covering ranges of $L_x = 30.0h$, $L_y = 5.0h$, and $L_z = 22.5h$ in the x (streamwise), y (spanwise), and z (vertical) directions, respectively. To absorb the perturbations caused by the grid changes at the beginning and end of the fine grid domain, the lengths of both the upstream and downstream fine grid regions were set to 15.0h, which was proven by Liu et al. [25,42] to be sufficiently long to absorb the perturbations caused by the boundaries. Within the fine grid region, the horizontal grid shape was square. Horizontal resolutions of 5.65 mm, 4.0 mm, 2.8 mm, and 2.0 mm were examined. The meshes with horizontal resolutions of 2.8 mm and 2.0 mm show almost the same results, indicating that a horizontal grid size of 2.0 mm yields grid-independent results. Therefore, in the fine grid region, a horizontal grid size of 2.0 mm was used. The grid-independence examination will be presented in section 2.6. Between the coarse grid region (the white area in Fig. 4) and the fine grid region (the dark gray area in Fig. 4), a buffer zone with a quadrilateral-shaped grid was considered, whose horizontal grid size increased with a growth factor of 1.2 from 2.0 mm at the boundary of the fine grid region to 10 mm at the inner boundary of the rough grid region, as represented by the light gray area in Fig. 4(a). A uniform grid with a size of 10 mm and square shape was applied in the coarse grid region.

In the vertical direction, the grid size of the first-layer grid was 0.005h, and the maximum growth ratio was 1.15. $y+$ on the surface of the target region was between 0.5 and 1.0. The total grid number was 24 million. Fig. 4(b) shows the vertical slices crossing the origin points of the 3D hills and 2D ridges.

The sizes and resolutions of our nested domains were chosen to make a compromise between the constraints related to the available computational time and the fact that the domain should be sufficiently large to represent the largest eddies and sufficiently fine to represent the smallest eddies of interest.

2.4. Boundary conditions

Stress-free conditions were used at the top of the domain ($\partial\tilde{u}/\partial n = 0$, $\partial\tilde{v}/\partial n = 0$, $\tilde{w} = 0$) and the spanwise sides ($\partial\tilde{u}/\partial n = 0$, $\partial\tilde{w}/\partial n = 0$, $\tilde{v} = 0$). Uniform wind flow with a constant speed of

Table 3
Case settings and computational resources.

Case name	Ground condition	Canopy height h_t (mm)	Topography shape	Reynolds number $Re = U_h h/\upsilon$	Horizontal grid size (mm)	N	Hours	CPU	Memory
Case0-1	Smooth	0.0	Flat	\	5.6	0.3×10^7	65	4 computers in parallel	64G
Case0-2	Smooth	0.0	Flat	\	4.0	0.6×10^7	123	Intel core i9-7980XE,	
Case0-3	Smooth	0.0	Flat	\	2.8	1.2×10^7	260	18 cores	
Case0-4	Smooth	0.0	Flat	\	2.0	2.4×10^7	491		
Case0′-1	Rough	5.0	Flat	\	5.6	0.3×10^7	75		
Case0′-2	Rough	5.0	Flat	\	4.0	0.6×10^7	136		
Case0′-3	Rough	5.0	Flat	\	2.8	1.2×10^7	296		
Case0′-4	Rough	5.0	Flat	\	2.0	2.4×10^7	563		
3Ds	Smooth	0.0	3D hill	1.7×10^5	2.0	2.4×10^7	634		
3Dr	Rough	5.0	3D hill	1.4×10^5	2.0	2.4×10^7	723		
2Ds	Smooth	0.0	2D ridge	1.7×10^5	2.0	2.4×10^7	761		
2Dr	Rough	5.0	2D ridge	1.4×10^5	2.0	2.4×10^7	793		

Table 4
Numerical schemes.

Time discretization scheme	Second-order implicit scheme	Smagorinsky constant Cs	0.1
Space discretization scheme	FVM second-order central difference scheme	SGS model	Smagorinsky-Lilly
$\Delta t U_h/h$	≈ 0.01	CFL number:	<2
Simulation method	LES	Decoupling method	SIMPLE
Time for statistics	20s	Software	Ansys Fluent 14.0

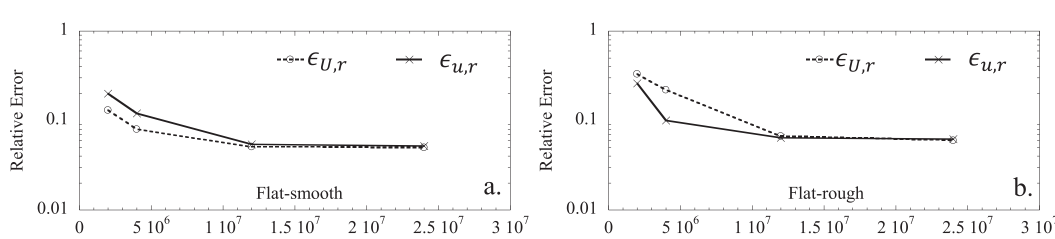

Fig. 5. Relative errors of mean streamwise velocity, $\varepsilon_{U,r}$, and rms of streamwise velocity, $\varepsilon_{u,r}$, versus grid number with horizontal axis increasing linearly and vertical axis increasing logarithmically. (a) smooth flat terrain, (b) rough flat terrain.

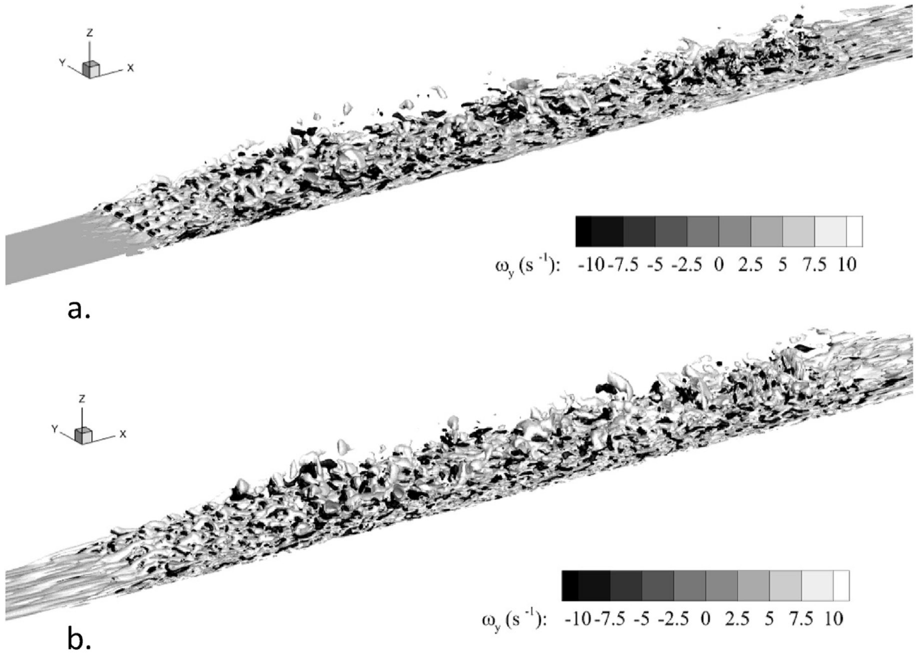

Fig. 6. Development of the boundary layer flow shown by vorticity of y component. (a) smooth ground condition of the flat terrain, (b) rough ground condition of the flat terrain.

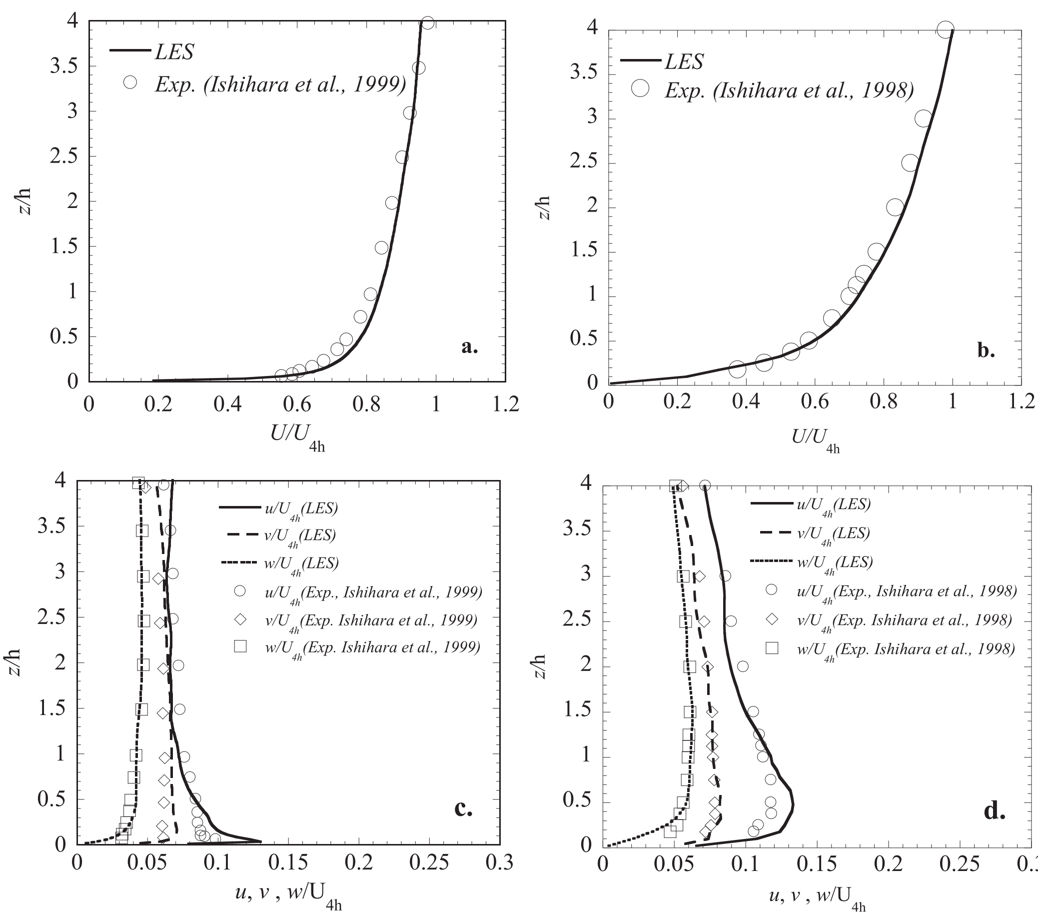

Fig. 7. Vertical profiles of the upcoming mean and fluctuating velocities. (a) normalized mean streamwise velocity with smooth ground, (b) normalized mean streamwise velocity with rough ground, (c) normalized fluctuating velocities with smooth ground, (d) normalized fluctuating velocities with rough ground. The experimental data from the study by Ishihara and Hibi [57] are superimposed to verified the accuracy of the upcoming boundary layer flow.

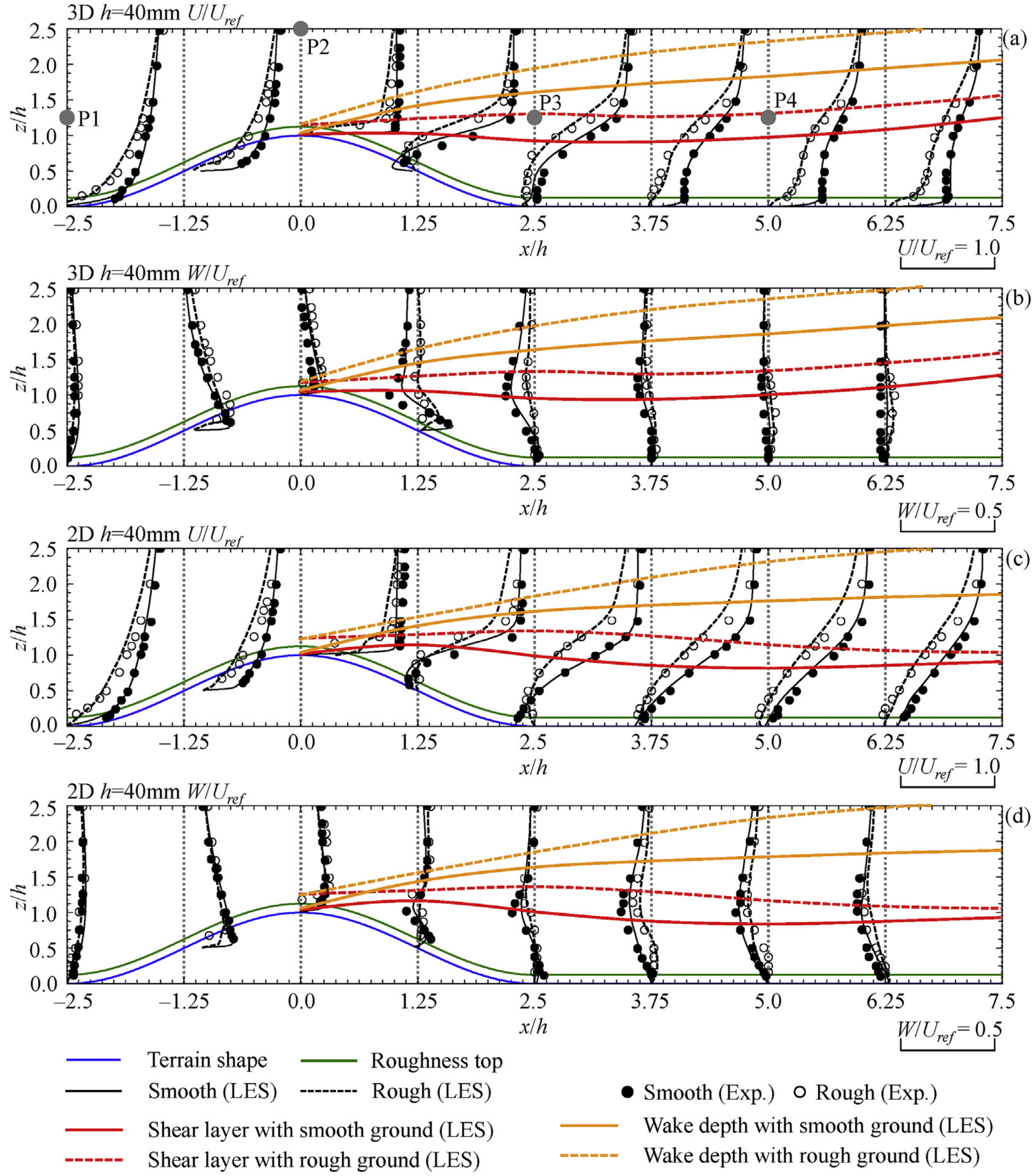

Fig. 8. Profiles of mean wind velocities on the *x-z* plane. *x* and *z* axis have been normalized by h. (a) profiles of *U* for 3D cases with smooth and rough ground, (b) profiles of *W* for 3D cases with smooth and rough ground, (c) profiles of *U* for 2D cases with smooth and rough ground, (d) profiles of *W* for 2D cases with smooth and rough ground. P1, P2, P3 and P4 are the four reference points for the calculation of two-point space correlation discussed in Section 4.1.

5.4 m s^{-1} in time was set at the inlet ($\partial\tilde{p}/\partial n = 0$, $\tilde{u} = 5.4$ m s^{-1}, $\tilde{v} = 0$, $\tilde{w} = 0$). At the end of the wind tunnel, outlet boundary conditions were applied, where the normal gradients of the pressure and velocities were 0 ($\partial\tilde{p}/\partial n = 0$, $\partial\tilde{u}_i/\partial n = 0$). Non-slip conditions were used at the bottom surface, where wall functions were applied ($\partial\tilde{p}/\partial n = 0$, $\tilde{u}_i = 0$). The boundary condition settings are listed in Table 2.

2.5. Solution scheme and solution procedure

In the numerical simulations, the variables were distributed in a non-staggered, cell-centered mesh system and the finite volume method was used. The second-order central difference scheme was utilized for the convective and viscous terms, and the second-order implicit scheme was employed for the unsteady term. The time step Δt was set to 0.0001 s, and in convective units, $\Delta t^* = \Delta t U_h/h \approx 0.01$, where U_h is the mean velocity at the point ($x = 0, y = 0, z = h$) when the ground is flat. For the smooth flat ground, $U_h = 4.37$ m s^{-1}, and for the rough flat ground, $U_h = 3.72$ m s^{-1}. The Reynolds number was defined as $Re = U_h h/\upsilon$. Re was 1.7×10^5 for the smooth topographies and 1.4×10^5 for the rough topographies. The solution method consisted of linearization of the non-linear equations and acquisition of a matrix solution. The predicted conjugate gradient method was applied to solve the linearized equations along with the algebraic multi-grid approach. The Courant–Friedrichs–Lewy (CFL) number [56] is based on Δt, the velocities $\tilde{u}_i$, and the grid size Δx_i and can be expressed as $C = \Delta t \Sigma \tilde{u}_i/\Delta x_i$. In this study, the CFL number did not exceed 2, $C_{\max} = 2$, throughout the computational domain. The semi-implicit pressure linked equations algorithm, which was introduced by Ferziger and Peric [52], was used to solve the discretized equations. Relaxation factors were employed to promote the stability of the process. These relaxation factors were

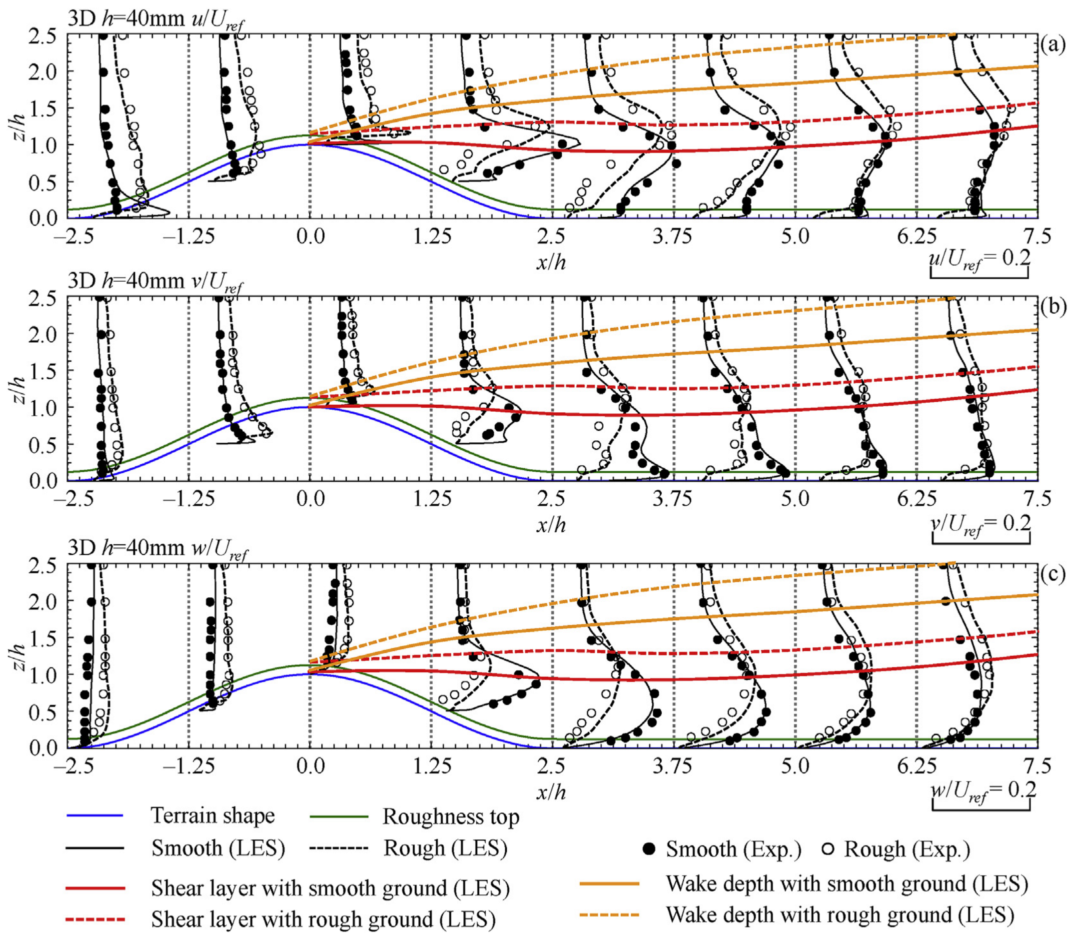

Fig. 9. Profiles of wind velocity fluctuations on the *x-z* plane for the 3D hill cases. *x* and *z* axis have been normalized by h. (a) profiles of *u* for 3D case with smooth and rough ground, (b) profiles of *v* for 3D cases with smooth and rough ground, (c) profiles of *w* for 3D case with smooth and rough ground.

0.3 and 0.7 for pressure and momentum, respectively. The commercial software Ansys Fluent 14.0 [57] was used for the calculations. Table 3 lists the settings for the various cases investigated in the present study.

The initial transient effects were found to disappear after 5 s. Therefore, the time sampling began at 10 s and the flow fields were averaged temporally from 10 s to 30 s. A stationary condition for time sampling could be achieved by evaluating the relative errors in the mean streamwise velocity at the point ($x=L,\ y=0,\ z=h$), which became less than 1% when the data from 10 s to 30 s were used. Consequently, the filtered wind velocity components in the LES, $\tilde{u}_i$, could be decomposed into $\tilde{u}_i = U_i + u_i'$, where U_i (U, V, W) denotes the time-averaged velocity and u_i' (u', v', w') is the deviation from the average value. The root-mean-square of u_i' represents the fluctuation of the velocity u_i (u, v, w). The simulations were performed on four PCs in parallel (Intel core i9-7980XE, 18 cores, 64G memory). Table 4 summarizes the numerical schemes adopted in the present study.

2.6. Grid independency

Four grid systems for smooth flat terrain (Cases 0-1 – 0-4) and four grid systems for rough flat terrain (Cases 0′-1 – 0′-4), with increasing horizontal refinement from 5.65 mm to 2 mm, as listed in Table 3, were constructed to conduct grid convergence tests. Except for the grid density, the settings were all the same. The U and u values obtained along the line ($x=L,\ y=0,\ h'=[0, 2h]$) using different mesh densities were compared, and the relative errors as functions of the grid number were analyzed. The relative errors were defined as follows. Firstly, the errors (ε_U for U and ε_u for u) were defined as the integrals of the absolute differences between the simulated results and the experimental data:

$$\varepsilon_U = \int_{0h}^{2h} \left| U_e(z) - U(z) \right| dz; \quad \varepsilon_u = \int_{0h}^{2h} \left| u_e(z) - u(z) \right| dz, \tag{12}$$

where U_e and u_e are the mean streamwise velocity and fluctuation, respectively, in the experiments by Ishihara and Hibi [58]. ε_U and ε_u were then normalized by the integrals of the experimental data to determine the relative errors:

$$\varepsilon_{U,r} = \frac{\varepsilon_U}{\int_{0h}^{2h} U_e(z)dz}; \quad \varepsilon_{u,r} = \frac{\varepsilon_u}{\int_{0h}^{2h} u_e(z)dz}. \tag{13}$$

As shown in Fig. 5, where a logarithmic scale is employed for the relative error axis, it can be seen that the relative errors are almost constant, 5.2% for Cases 0–3 and 0–4 and 6.3% for Cases 0′-3 and 0′-4, which means that grid independence was achieved.

The grid-independent boundary layer flow fields over flat terrains are presented in Fig. 6, where it can be seen clearly that even when the roughness blocks were not directly built, the turbulence

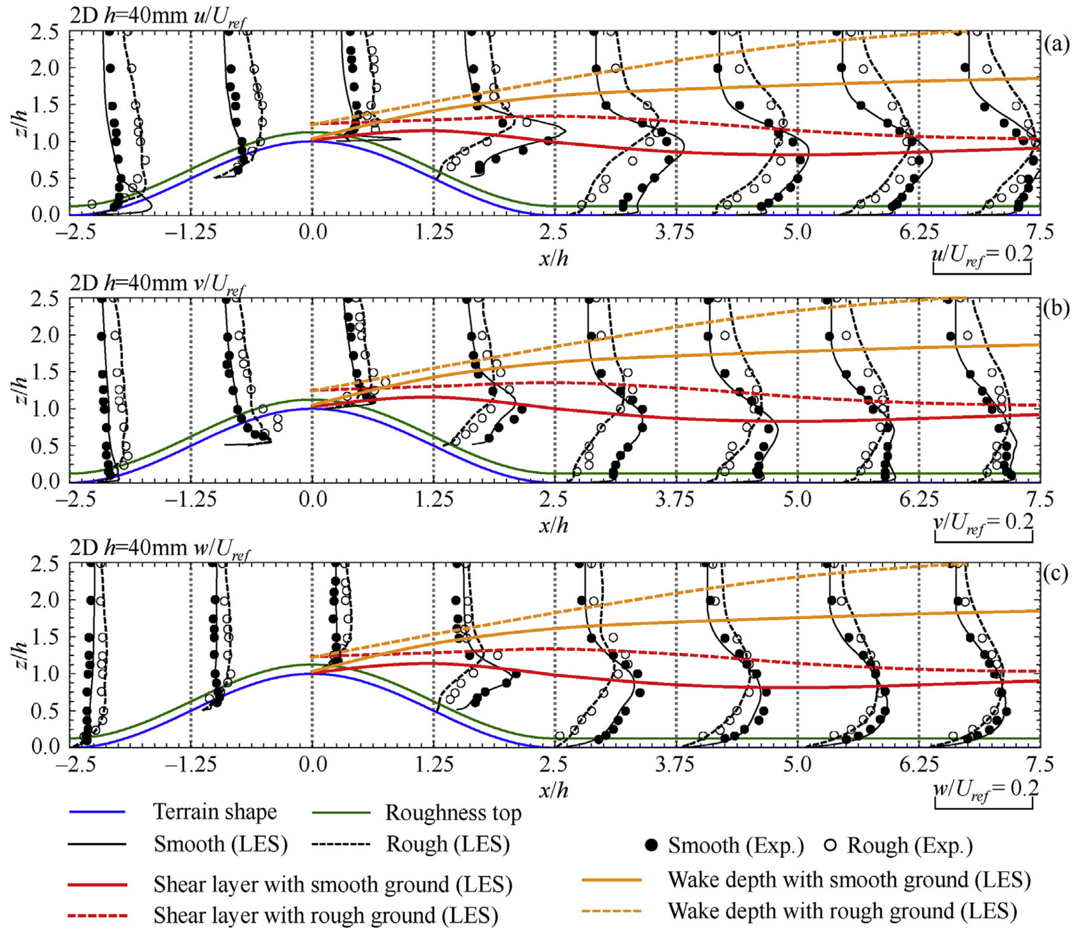

Fig. 10. Profiles of wind velocity fluctuations on the *x-z* plane for the 2D hill cases. *x* and *z* axis have been normalized by h. (a) profiles of *u* for 2D case with smooth and rough ground, (b) profiles of *v* for 2D cases with smooth and rough ground, (c) profiles of *w* for 2D case with smooth and rough ground.

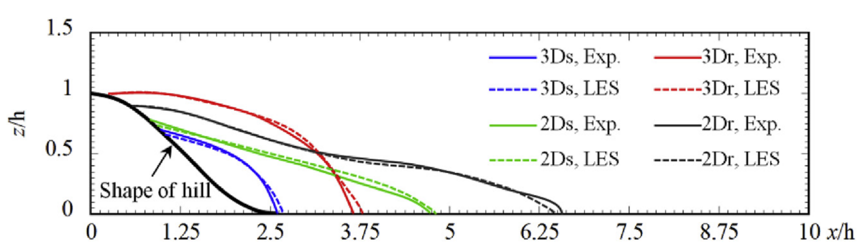

Fig. 11. Shape of the separation bubble. Solid lines are from the experiments by Ishihara and Hibi [57] and the dashed lines are from the present LES calculations. *x* and *z* axis have been normalized by h.

flow could be generated successfully. The turbulence develops as soon as the flow touches the roughness blocks, and the boundary layer thickness increases as the flow propagates. In addition, the boundary layer flow is much more turbulent when the ground is rough.

Fig. 7 shows the comparison of mean and fluctuating velocity profiles between the present simulation and the experiments by Ishihara and Hibi [58] for the upcoming flow. The vertical coordinate is normalized by *h* and the mean velocities are normalized by U_{4h}, which is the mean velocity at the height of 4 h when the terrain is flat. The generated upcoming turbulent boundary layer flow show good agreement with the experiment validating the accuracy of modeled upcoming flow. The vertical profiles of mean velocities as well as three components of fluctuations at the locations of $x=-0.25$ m, $y=0$ and $x=0.25$ m, $y=0$ are also extracted and compared with those at $x=0$, $y=0$. The comparisons between them are in good agreement (not shown in the figure), implying a fully developed and stable boundary layer.

3. Validation of the numerical data

Before discussing the numerical results related to the coherent flow structures for all four topographies with different roughness conditions, the validation of the LES results, which was performed by comparing the mean flow fields as well as the fluctuations of the wind velocities with those measured experimentally, will be presented. The comparison was on the symmetric plane ($y=0$) for each configuration. In the present study, the height of the shear layer center h_s was determined by connecting the peaks of the fluctuating streamwise velocities. Following the definition provided by Kaimal and Finnigan [59], the upper limit of the wake depth was calculated as the height at which the mean streamwise velocity was equal to the value upstream of the hill at the same height. In the present study, the wake depth h_w was quantitatively calculated using $|U_{down}(h_w) - U_{up}(h_w)|/U_{up}(h_w) < 0.01$, where U_{down} and U_{up} are the mean streamwise velocities downstream and upstream from the topography, respectively.

3.1. Mean velocities

Fig. 8 show the vertical profiles of time-averaged streamwise and vertical velocity components, U and W, respectively, for the four configurations (3Ds, 3Dr, 2Ds, and 2Dr). In order to compare with the experiment by Ishihara and Hibi [58], the mean streamwise velocity at the height of 4 h, U_{ref}, in absence of hills are chosen to do normalization in Figs. 8–10. Qualitatively, several features appear to have been reproduced very well. Firstly, a strong shear layer forms immediately downstream from the top of the topography in each case. Secondly, the reversed flow regions in the smooth cases (3Ds and 2Ds) are much smaller than those in the corresponding rough cases (3Dr and 2Dr). Thirdly, within the turbulent boundary layer, increased roughness decreases U_i in the surface layer and leads to earlier flow separation, resulting in considerable recirculation. Finally, the downstream extents of the recirculating regions of the 2D ridges are longer than those of the 3D hills. The quantitative accuracy of the U_i results obtained using the LES is good. Upstream from the summit of the topography ($x < 0h$) and in the far wake region ($x > 3.75h$), the LES results almost coincide with the experimental results. The largest $\varepsilon_{U_i,r}$ values (determined by using Eq. (13)) in these two regions among all of the configurations are only 3.2% for U, which occurs at $x = 3.75h$ in the 2Ds case, and 4.5% for W, which occurs at $x = 3.75h$ in the 2Dr case. The discrepancies are concentrated in the near wake region ($0h < x < 3.75h$) for both U and W. The largest $\varepsilon_{U_i,r}$ values in the near wake region are 7.6% for U, which occurs at $x = 1.25h$ in the 2Ds case, and 8.2% for W, which occurs at $x = 1.25h$ in the 2Dr case.

3.2. Wind velocity fluctuations

Figs. 8 and 9 show the vertical profiles of the normalized wind velocity fluctuations in the x-direction (u), y-direction (v), and z-direction (w). Generally, the LES data are comparable to the experimental data. Qualitatively, several important features of the velocity fluctuations appear to have been modeled successfully. For u, the sole peaks in the profiles are clear. Meanwhile, there are two peaks in each v profile, with the upper one located at the height of the corresponding u peak and the lower one located very close to

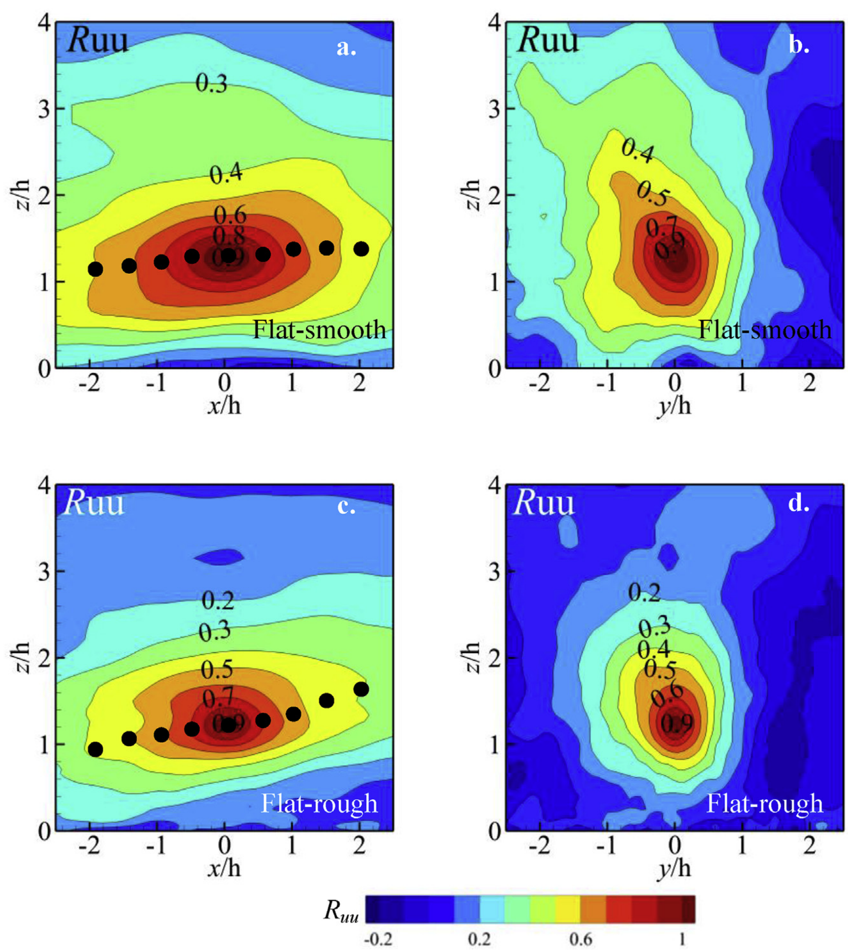

Fig. 12. Two-points space correlations for the flat terrains on x-z plane and y-z plane. x, y and z axis have been normalized by h. The reference point is at the height of 1.25 h. (a) R_{uu} of smooth flat terrain on x-z plane, (b) R_{uu} of smooth flat terrain on y-z plane, (c) R_{uu} of rough flat terrain on x-z plane, (b) R_{uu} of rough flat terrain on y-z plane. The reference point is at the height of h. Solid circles, ●, indicate the peak of R_{uu}.

the ground. The w profiles peak at heights lower than those of the u peaks. In addition, the much sharper increases of u, much clearer pairs of peaks in the v profiles, and higher locations of the u and w peaks after introducing vegetation on the ground that were found in the experiments were well reproduced by the LES. The quantitative accuracy of the LES for the fluctuations is satisfactory. Above h_w and below h_s, the LES predictions agree well with the experimental results. However, for all of the configurations and all of the components, the discrepancies are relatively large in the region between h_w and h_s. In this region, the u, v, and w values predicted by the LES are always larger than those obtained experimentally, with maximum $\varepsilon_{u_i,r}$ values (determined by using Eq. (13)) of 12.6% for u, which occurs at $x = 5h$ in the 3Ds case; 14.2% for v, which occurs at $x = 3.75h$ in the 3Ds case; and 12.6% for w, which occurs at $x = 2.5h$ in the 2Dr case. These errors may have resulted from the fact that in the regions above h_w and below h_s, the flow is fully developed boundary layer flow, but the area between h_w and h_s is a transient region in which both the strength and structure of the turbulence change quickly, which is difficult for the LES turbulence model to reproduce accurately.

3.3. Recirculation bubble

The region of the recirculation bubble was determined by connecting the reverse points on the vertical U profiles following the procedure employed by Ishihara [60]. The recirculation bubbles obtained using the present LES and by Ishihara [60] are compared in Fig. 11, from which it can be found that introducing vegetation on the ground expands the recirculation bubble significantly in both the vertical and horizontal directions. Furthermore, changing the shape of the topography from a 3D hill to a 2D ridge also expands the recirculation bubble, but mainly does so in the streamwise direction. These features were successfully captured by the present LES. The bubble size was also predicted very well, with a maximum error in the streamwise direction of only 5.3%, which occurs in the 3Dr case, and a maximum error in the vertical direction of only 6.2%, which occurs in the 2Ds case.

3.4. Summary of the validations

From the above comparison of U_i, u_i, and the recirculation bubble shape, it can be seen that LES can be used to predict mean flow fields but will produce errors in the fluctuations. In some cases, $\varepsilon_{u_i,r}$ could reach about 15%, whereas in engineering applications, 10% is always the maximum allowed error. However, flow fields are very complicated in wake regions. For instance, although Ishihara and Hibi [58] utilized a split fiber, whose influence on a flow field is much less than that of an X-wire, to perform their experimental measurements, the complicated flow fields in the wake were still very sensitive to the appearance of the measurement device. In addition, the main purpose of the present study was to clarify the differences in the coherent flow structures over typical topographies with different ground roughness conditions. Therefore, the relatively large errors of the fluctuations in the wake

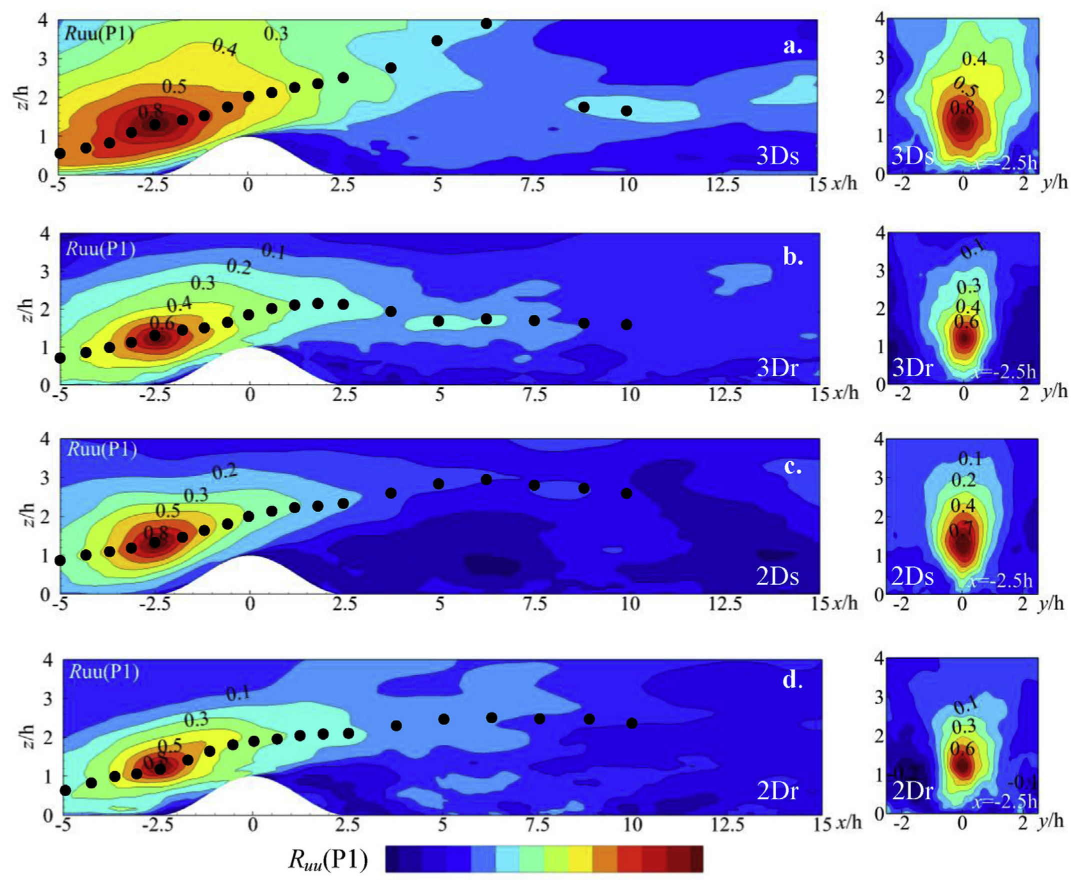

Fig. 13. Two-points space correlations, R_{uu}(P1), for the flat terrains on x-z plane and y-z plane. x, y and z axis have been normalized by h. The figures on the left hand side are the distributions on x-z plane and the figures on right hand side are the distributions on y-z plane. (a) R_{uu} of 3Ds, (b) R_{uu} of 3Dr, (c) R_{uu} of 2Ds, (d) R_{uu} of 2Dr. The reference point is at the height of h. Solid circles, ●, indicate the peak of R_{uu}.

regions can be considered to be acceptable. Consequently, it can be concluded that the LES predictions obtained in the present study are satisfactory overall.

4. Coherent structures of the turbulent flow

The turbulence flow fields over topographies, including the mean velocities, fluctuations, and kinetic energy, have been studied widely by researchers in the fields of wind engineering [25,29,30,33,42], atmospheric science [61–65], and fluid mechanics [66,67]. However, the influences of the shape of the topography as well as the ground roughness conditions on coherent turbulent structures have not been examined. In this section, the zero time-lag two-point correlations $R_{u_iu_i}$, skewness Sku_i, kurtosis Kuu_i, PSD S_{ui}, turbulent length scale Lu_{xi}, E, and Q are addressed. Before discussing these parameters in detail, it is meaningful to provide their detailed definitions.

(a) $R_{u_iu_i}$ provides spatial information related to the size of the main turbulent structure. This parameter has been applied to wind-tunnel experiments [68], field observations [69], and LES modeling [54,70]. $R_{u_iu_i}$ is determined using the following expression:

$$R_{u_iu_i}(x,\ y,\ z) = \frac{u_i(x,\ y,\ z)u_i\left(x_{ref},\ y_{ref},\ z_{ref}\right)}{u_i(x,\ y,\ z)\cdot u_i\left(x_{ref},\ y_{ref},\ z_{ref}\right)}. \tag{14}$$

Here, (x_{ref}, y_{ref}, z_{ref}) are the coordinates of the reference points (P1, P2, P3, and P4), which are depicted as red points in Fig. 8(a).

(b) The skewness of u_i, $Sku_i = u_i^3/(u_iu_i)^{3/2}$, provides information about the symmetry of the PDF of u_i. It should be noted that the skewness of any univariate normal distribution is 0.

(c) The kurtosis of u_i, $Kuu_i = u_i^4/(u_iu_i)^2$ denotes the peakedness of the sampled events. It should be noted that the kurtosis of any univariate normal distribution is 3. In addition, the kurtosis should never be less than 1 and will be 1.8 if the PDF is uniform.

(d) The maximum-entropy method (MEM) can be used to smooth S_u. The MEM is a spectral density estimation technique based on the extrapolation of a segment of a known autocorrelation function with unknown lags [71–73].

(e) Lu_{xi} is another important parameter, which represents the size of the major vortices in the fluid and is always calculated by integrating the self-correlation function. For the streamwise component, Lu_x can be expressed as

$$Lu_x = \frac{U}{u^2}\int_0^{R_u(\tau)=0.05u^2} R_u(\tau)d\tau, \tag{15}$$

where $R_u(\tau)$ is the self-correlation function and τ is the time lag.

(f) The local rotation rate of the flow can be quantified using E, i.e., half of the square of the vorticity, $E = 1/2\omega_i\omega_i$, where ω_i is the instantaneous vorticity component of the flow along x_i, $\omega_i = (\partial\tilde{u}_j/\partial x_k - \partial\tilde{u}_k/\partial x_j)$.

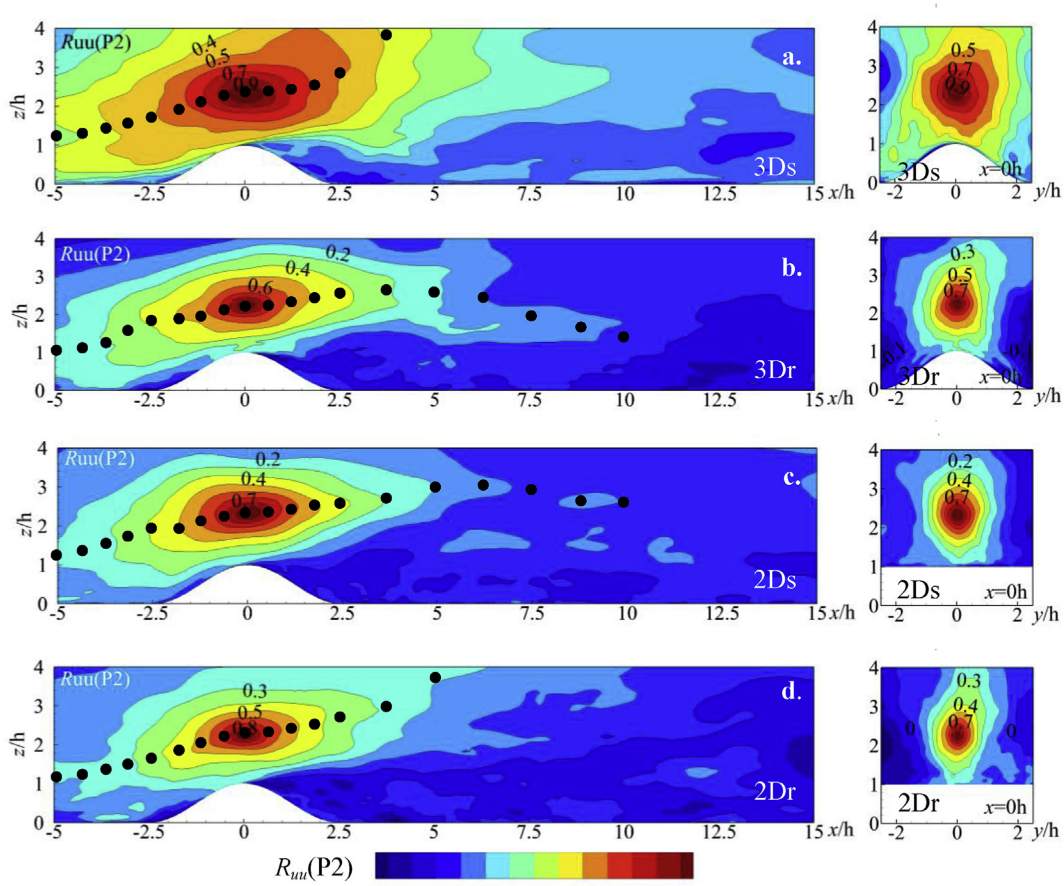

Fig. 14. Two-points space correlations, R_{uu} (P2), for the flat terrains on x-z plane and y-z plane. x, y and z axis have been normalized by h. The figures on the left hand side are the distributions on x-z plane and the figures on right hand side are the distributions on y-z plane. (a) R_{uu} of 3Ds, (b) R_{uu} of 3Dr, (c) R_{uu} of 2Ds, (d) R_{uu} of 2Dr. The reference point is at the height of h. Solid circles, ●, indicate the peak of R_{uu}.

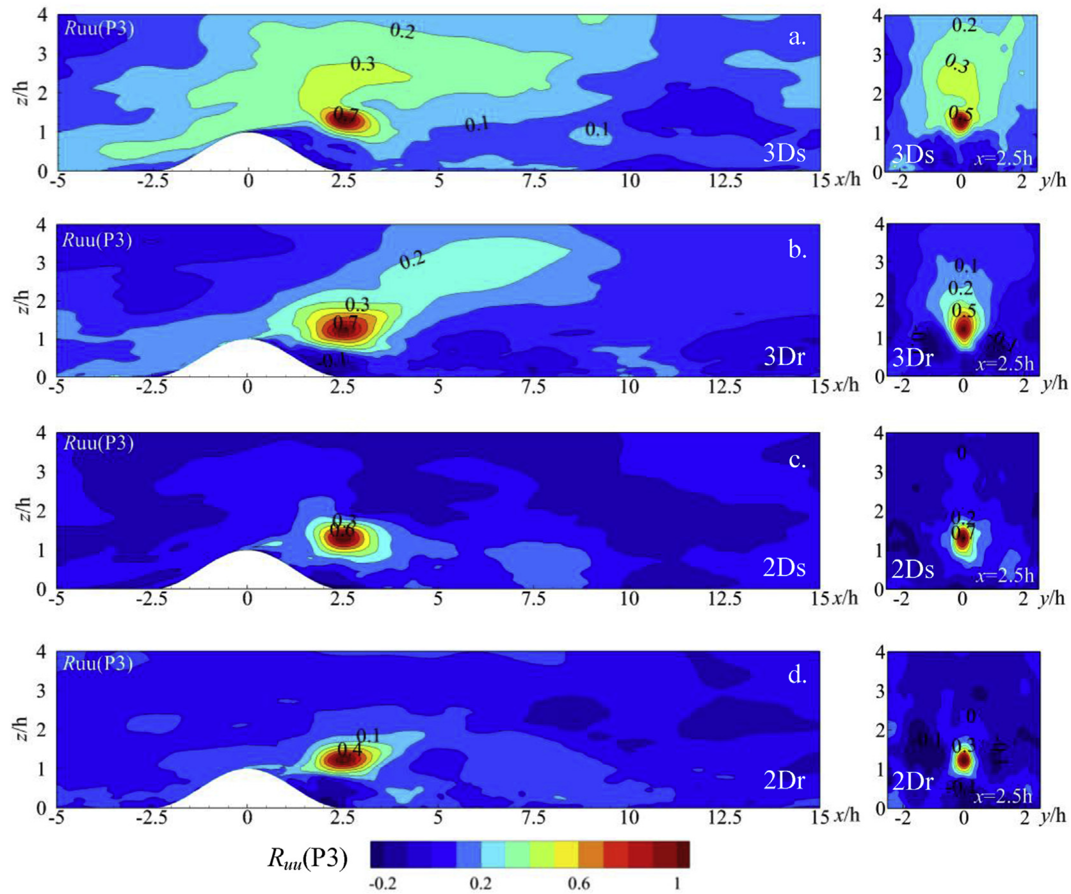

Fig. 15. Two-points space correlations, R_{uu} (P3), for the flat terrains on *x-z* plane and *y-z* plane. *x*, *y* and *z* axis have been normalized by h. The figures on the left hand side are the distributions on *x-z* plane and the figures on right hand side are the distributions on *y-z* plane. (a) R_{uu} of 3Ds, (b) R_{uu} of 3Dr, (c) R_{uu} of 2Ds, (d) R_{uu} of 2Dr. The reference point is at the height of h.

(g) Q quantifies the relative amplitude of the rotation rate as well as the strain rate of the flow. It helps with vortex core identification. $Q = 1/2(S_{ij}S_{ij} - \Omega_{ij}\Omega_{ij})$, where $S_{ij} = 1/2(\partial\tilde{u}_i/\partial x_j - \partial\tilde{u}_j/\partial x_i)$ and $\Omega_{ij} = 1/2(\partial\tilde{u}_i/\partial x_j + \partial\tilde{u}_j/\partial x_i)$ are the antisymmetric and symmetric components, respectively, of the velocity-gradient tensor.

Only the streamwise components of $R_{u_iu_i}$, Sku_i, Kuu_i, S_{ui}, and Lu_{xi} (R_{uu}, Sk_u, Ku_u, S_u, and Lu_x, respectively) were considered, because the streamwise component strongly influences not only the mean velocity, but also the fluctuating part.

4.1. R_{uu}

To serve as reference data for the discussion of the influences of the topography and ground roughness, the distributions of R_{uu} on the $y = 0$ and $x = 0$ planes for flow over flat ground are presented in Fig. 12. The reference point is at a height of 1.25h. Both smooth and rough ground conditions are considered. The height of 1.25h was selected considering that, in the wake regions of the topographies in the present study, high turbulence was located at about $h' = 1.25h$. With smooth ground, the distribution of R_{uu} is almost symmetric about the axis $y = 0$. Thus, if the distance from the reference point is the same, R_{uu} will be the same upstream and downstream from the reference point at the same height. However, the distribution is not symmetric in the vertical direction. R_{uu} is concentrated more in the region above the reference point due to the high wind velocity. In addition, R_{uu} is much stronger in the streamwise direction than in the vertical direction, resulting in an elliptical shape. When the vegetation is introduced on the ground, some interesting features emerge. Firstly, R_{uu} is weaker than it is with smooth ground. Secondly, the distribution of R_{uu} on the $y = 0$ plane becomes tilted. The latter phenomenon is not considered in most widely used correlation functions, such as IEC [6,74]. This tilted shape of the correlated area is consistent with those previously observed over homogeneous canopies in wind tunnel experiments [68], field observations [69], and LES studies [54,70].

The curvature of the topography changes the shapes of the contours of R_{uu} considerably, as can be seen in Figs. 13–16, where the solid circles indicate the locations of peak R_{uu}, and the reference points for Figs. 13–16 are P1, P2, P3, and P4, respectively. In Figs. 13–16, the plots on the left- and right-hand sides correspond to the *x-z* and *y-z* planes, respectively.

For P1 (see Fig. 13), if the ground is smooth, introducing a 3D hill shape or 2D ridge shape causes the correlated contours to be more tilted toward to the ground due to the sloping of the topography. The correlated area is larger for the 3D smooth hill than for the 2D smooth ridge. In the rough cases, the additional turbulence generated by the vegetation disturbs the flow further. Consequently, both the longitudinal and vertical sizes of the correlated areas are smaller than those in the corresponding smooth cases. In all four cases, the downstream parts of the R_{uu} contours extend only above the wake region, and due to the reversed flow in the

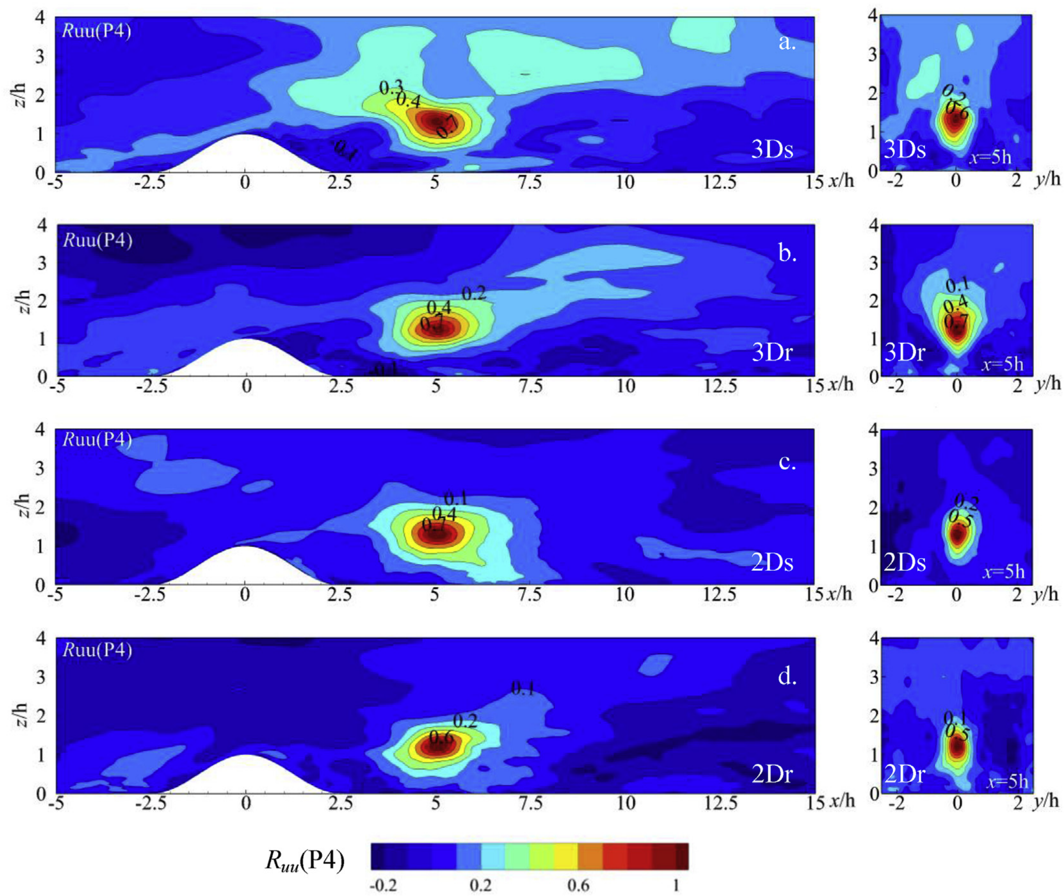

Fig. 16. Two-points space correlations, R_{uu}(P4), for the flat terrains on *x-z* plane and *y-z* plane. *x*, *y* and *z* axis have been normalized by h. The figures on the left hand side are the distributions on *x-z* plane and the figures on right hand side are the distributions on *y-z* plane. (a) R_{uu} of 3Ds, (b) R_{uu} of 3Dr, (c) R_{uu} of 2Ds, (d) R_{uu} of 2Dr. The reference point is at the height of h.

separation bubble, a region with anticorrelation is evident.

At P2, as shown in Fig. 14, owing to the decrease in the slope of the topography, the tilt of the correlated area decreases. The longitudinal and vertical sizes of the correlated area exhibit no obvious differences from those at P1. In the spanwise direction, the correlated area is clearly larger for the 3D hill cases, indicating some coherent turbulence generated by the 3D hills. In the wake region, R_{uu} is nearly 0, except in the recirculation bubble, which means the wind fields near P2 are not at all correlated with the wind field in the wake region. This finding also implies that the strong turbulent structure upwind from the summit is mostly advected above h_W. The animation developed based on the LES data revealed some cases of strong structures coming from upwind and entering the wake region, but their occurrence was rare.

Just downstream from the top of the hill, as shown in Fig. 15, the correlated area of R_{uu}(P3) is considerably smaller than those of R_{uu}(P1) and R_{uu}(P2). R_{uu}(P3) is mostly confined to within the shear layer region, and the longitudinal size is only about one-third of those of R_{uu}(P1) and R_{uu}(P2), implying the existence of very small turbulent structures. The effects of the shape of the topography and ground conditions remain, i.e., changing the topography from a 3D hill to a 2D ridge or changing the ground from smooth to rough decreases the correlated area. Interestingly, the correlation is quite strong above the reference point but decreases very quickly closer to the ground in the 3D hill cases. However, in the 2D ridge cases, the correlation decreases at nearly the same rate in four directions (+*y*, -*y*, +*z*, and -*z*), forming nearly circular contours.

Further increasing the distance of the reference point from the summit of the topography (P4) enables the correlated area to be recovered, as shown in Fig. 16. Both the tilt and size of the correlated area become nearly the same as those in the corresponding flat cases, indicating a weakening of the effects of the topography on the turbulence structures. Furthermore, for all of the cases, all of the locations, and all of the reference points, R_{uu} covers a larger area in the streamwise direction than in the vertical and spanwise directions, indicating that R_{uu} is also a function of the direction.

4.2. Sk_u and Ku_u

As shown in Fig. 17, Sk_u is negative in the case of free stream flow and becomes positive close to the ground in the wake of the hill, but above *h*, the skewness is around 0.6, which is close to the skewness of the Rayleigh distribution in the study by Celik [75]. In the smooth ground cases (3Ds and 2Ds), a region of large skewness ($Sk_u < -1.5$) is clearly evident, which always occurs in the wake of the cylinder [76,77], implying that there should be clear coherent turbulence structures in the wakes of smooth 3D hills and smooth 2D ridges. A large negative Sk_u means an asymmetric distribution of wind velocity around its mean value, with a greater probability of strong wind events. It should be noted that in the 3Ds case, there exists another zone, $2.5h < x < 7.5h$, $z < 0.3h$, with high positive skewness, $Sk_u > 0.5$, which is not evident in the 2Ds case. In the 2Ds case, Sk_u is almost 0 in the wake region, indicating a symmetric PDF distribution. After introducing vegetation on the ground, the region with

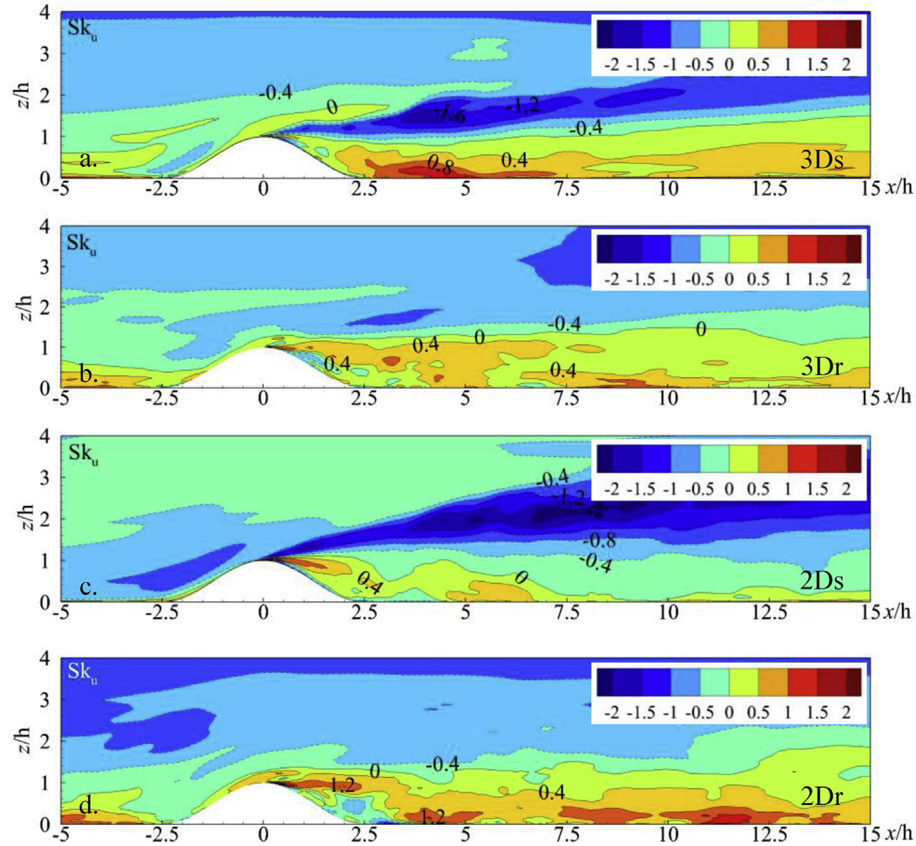

Fig. 17. Skewness of streamwise velocity on x-z plane. x and z axis have been normalized by h. (a) Sk_u for 3Ds case, (b) Sk_u for 3Dr case, (c) Sk_u for 2Ds case, (d) Sk_u for 2Dr case.

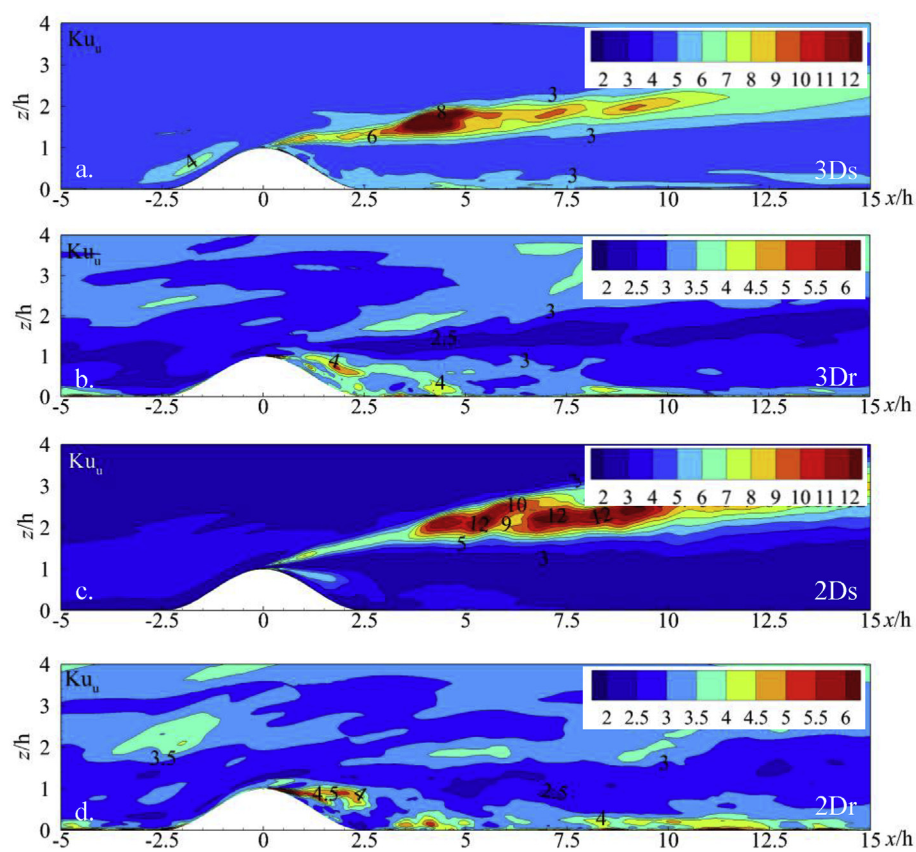

Fig. 18. Kurtosis of streamwise velocity on x-z plane. x and z axis have been normalized by h. (a) Ku_u for 3Ds case, (b) Ku_u for 3Dr case, (c) Ku_u for 2Ds case, (d) Ku_u for 2Dr case.

large negative skewness disappears. For Ku_u, as shown in Fig. 18, the kurtosis is close to 3 in most regions when the ground is covered by vegetation, indicating a normal PDF distribution. Meanwhile, when the ground is smooth, large kurtosis centered in the shear layer region is evident.

The skewness and kurtosis of a PDF are the two most important parameters in determining its shape, and wind velocity PDFs are important for calculating the fatigue loads of wind-resistant structures. Based on the above examination, it is apparent that both the shape of the topography and ground roughness can affect the PDF shape. Consequently, when determining wind-induced fatigue loads, the Weibull distribution, which is widely used to calculate fatigue loads, should be employed cautiously, especially for the shear layer region where quite large Ku_u and negative Sk_u occur.

4.3. S_u and Lu_x

To analyze the dynamics of the eddy motions, the time histories of the velocities at several locations, i.e., $x = -2.5h$, $x = 0.0h$, $x = 2.5h$, and $x = 5.0h$, were recorded and spectral analysis was conducted for the streamwise component S_u. S_u was normalized against a non-dimensional frequency $f = nh/U_h$, where n is the natural frequency in hertz.

To verify the oncoming flow and provide reference data for the following discussion of the dynamics of the eddy motions in the near-wake regions of the 3D hills and 2D ridges, the PSDs of u' for the flat ground cases are plotted in Fig. 19. From these plots, it can be seen that the normalized power spectra at $x = 0$, $y = 0$, $z = h$ display a slope of $-5/3$ in the inertial sub-range, as predicted by Kolmogorov [78]. For the smooth flat ground case, the data obtained experimentally at h by Ishihara et al. [29] are available. The simulated results agree well with these experimental data. The simulated peak frequency, $f = 0.055$, is shifted slightly toward the low frequency range. This agreement indicates that not only the turbulence statistics but also the dynamics of eddy motions are well reproduced for the oncoming flow. Interestingly, the S_u profiles shift toward higher frequencies with increasing elevation in the smooth flat ground case. The reverse is true in the rough case, where the S_u peaks cover a wider range, which is indicated by two vertical dashed lines in Figs. 19–23.

Introducing curved topography can affect the S_u distribution considerably even at $x = -2.5h$, as shown in Fig. 20, and the greatest influence occurs in the 3Ds case. In that case, the tendency of the S_u

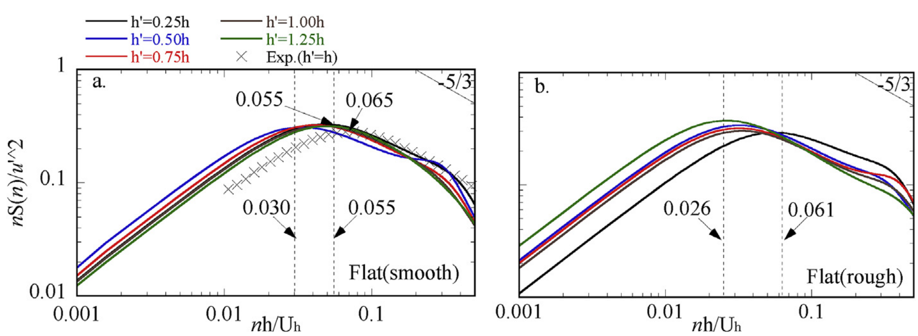

Fig. 19. Spectrum of streamwise velocities for the cases of (a) smooth flat terrain and (b) flat rough terrain. The cross symbols, ×, are the data from the experiments by Ishihara et al. [29]. The dashed lines are the boundaries of the spectrum peaks.

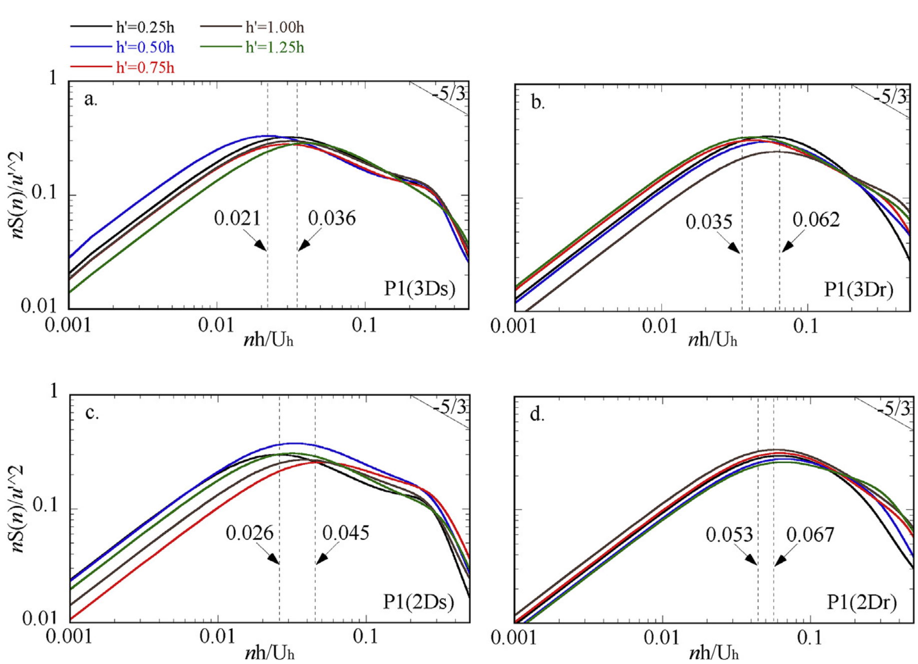

Fig. 20. Spectrum of streamwise velocities at $x = -2.5$ h for the cases of (a) 3Ds, (b) 3Dr, (c) 2Ds and (d) 2Dr. The dashed lines are the boundaries of the spectrum peaks.

profiles to move toward higher frequencies with increasing elevation is still obvious; however, the lowest peak occurring at $h' = 0.5h$ and the highest peak occurring at $h' = 1.25h$ are reduced to 0.021 and 0.036, respectively. Except in the 3Ds case, a substantial effect can also be found for the 2D ridge cases, where the PSD becomes more concentrated. In addition, the peak frequencies of the PSDs are higher for the 2D ridges than for the corresponding 3D hills, which implies that 2D ridges have greater disturbing effects than 3D hills. Moving to $x = 0.0h$, which is just above the summit of the topography in each case, there are only tiny changes in the PSDs compared with those at $x = -2.5h$ (see Fig. 21). However, in the near wakes of the topographies, $x = 2.5h$, sudden changes in the PSDs are clearly evident, as shown in Fig. 21. Firstly, the peak frequencies at $x = 2.5h$ for the 3D hill cases are increased by almost two times compared to those at $x = 0.0h$, indicating the existence of high frequency vortices generated by the hills. Secondly, for the 3D hill cases, S_u becomes more concentrated and the profiles are much steeper, which implies the existence of a coherent turbulence structure in the wake. This PSD concentration was also observed experimentally by Ishihara et al. [29], whose data are superimposed in Fig. 22(a). The simulated and experimental results agree well. Some slight discrepancies were caused by the difference between

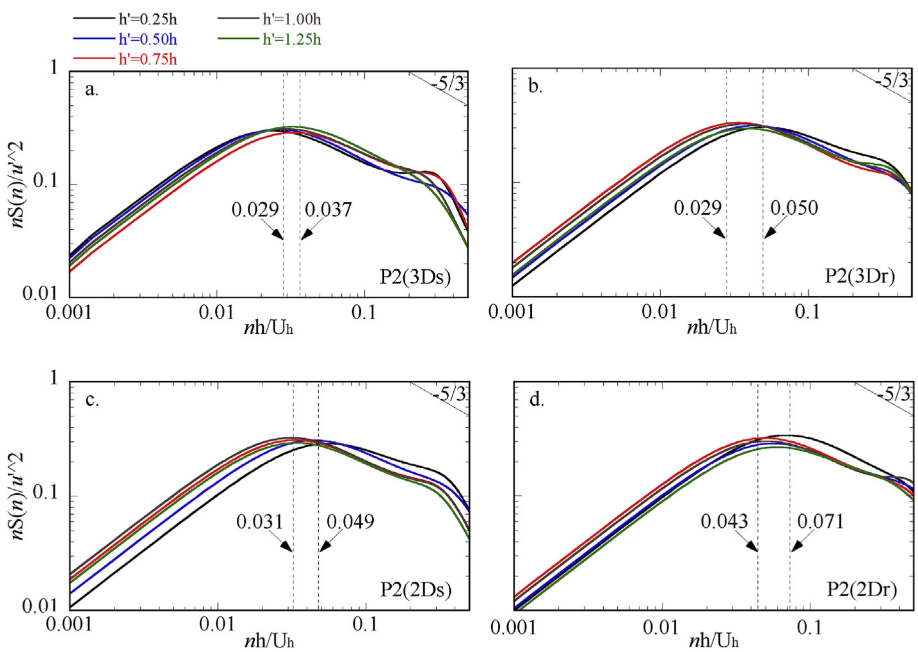

Fig. 21. Spectrum of streamwise velocities at $x = 0.0$ h for the cases of (a) 3Ds, (b) 3Dr, (c) 2Ds and (d) 2Dr. The dashed lines are the boundaries of the spectrum peaks.

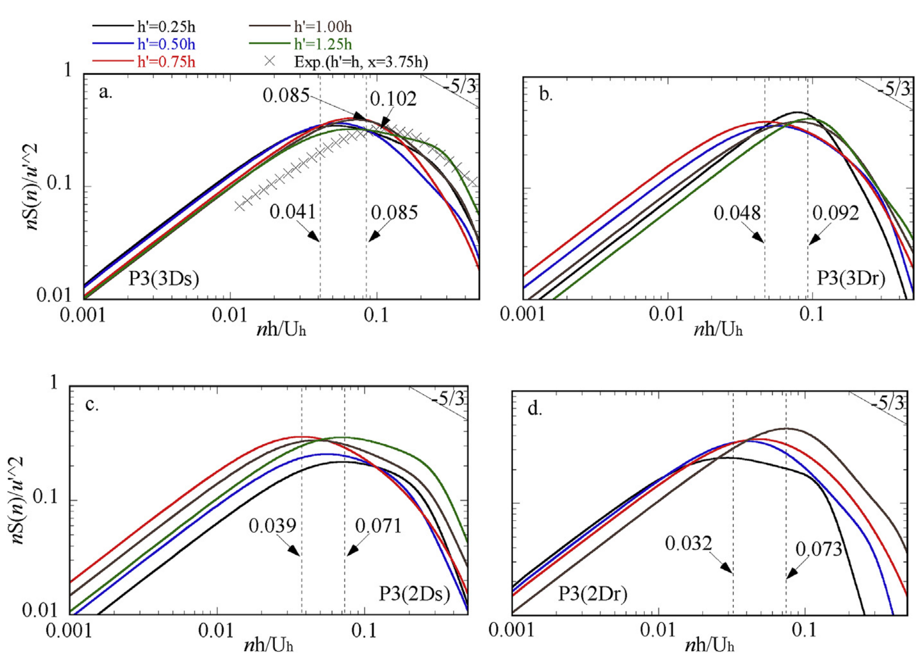

Fig. 22. Spectrum of streamwise velocities at $x = 2.5$ h for the cases of (a) 3Ds, (b) 3Dr, (c) 2Ds and (d) 2Dr. The cross symbols, ×, are the data at $h' = $ h and $x = 3.75$ h from the experiments by Ishihara et al. [29]. The dashed lines are the boundaries of the spectrum peaks.

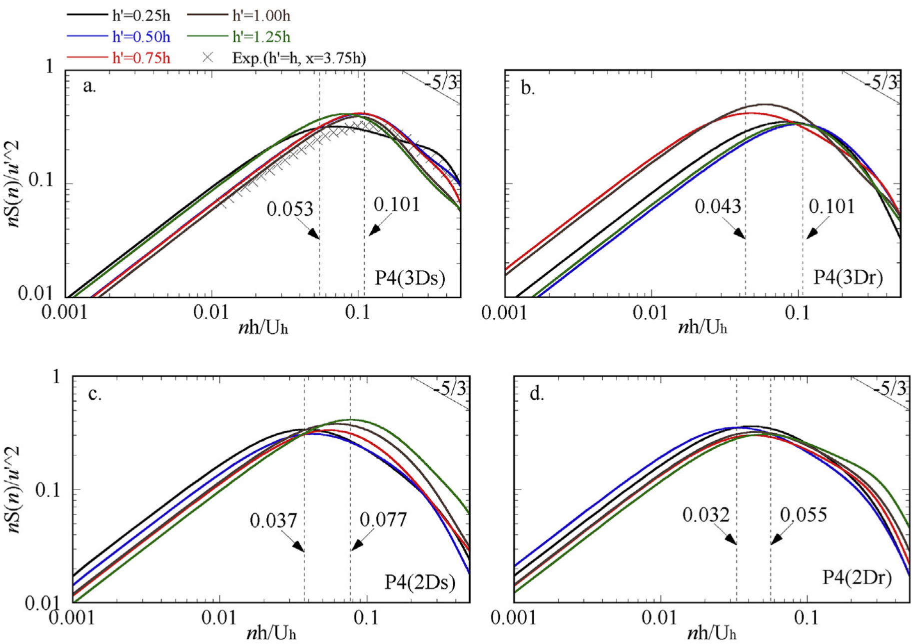

Fig. 23. Spectrum of streamwise velocities at $x = 5.0$ h for the cases of (a) 3Ds, (b) 3Dr, (c) 2Ds and (d) 2Dr. The cross symbols, ×, are the data at $h' = $ h and $x = 3.75$ h from the experiments by Ishihara et al. [29]. The dashed lines are the boundaries of the spectrum peaks.

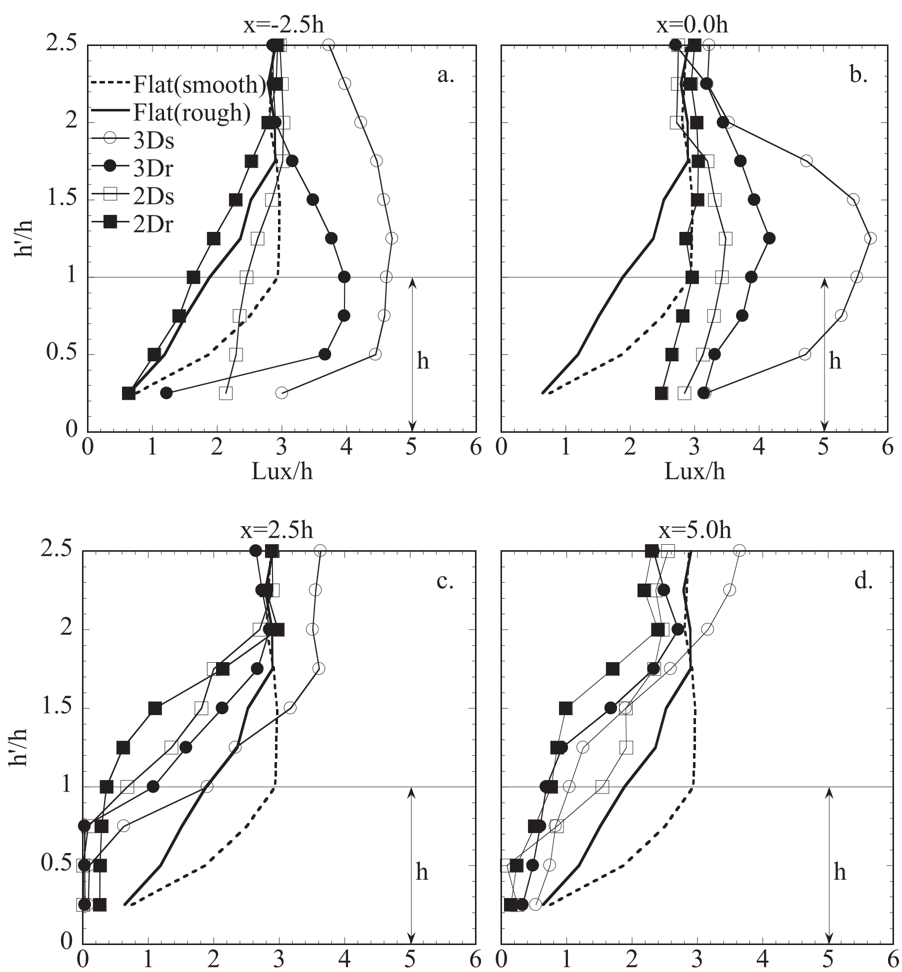

Fig. 24. Turbulence length scales at locations of (a) $x = -2.5$ h, (b) $x = 0.0$ h, (c) $x = 2.5$ h and (d) $x = 5.0$ h. The height and the turbulence length scales are normalized by h. Horizontal thin lines show the height of the topographies.

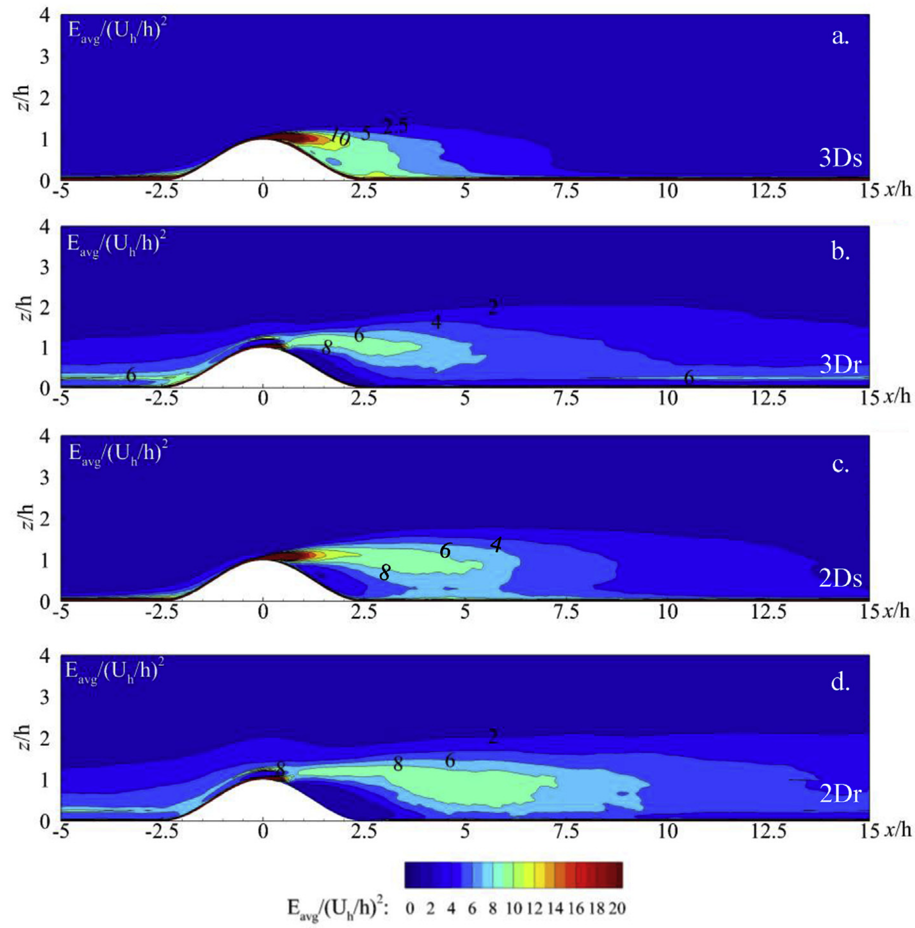

Fig. 25. Distributions of mean enstrophy on *x*-*z* plane. (a) 3Ds, (b) 3Dr, (c) 2Ds and (d) 2Dr. E_{avg} has been normalized by U_h^2/h^2. *x* and *z* axis have been normalized by h.

the observing points employed in the two cases; in the experiment, the point was at $x = 3.75h$, while it was at $x = 2.5h$ in the LES. The same comparison was conducted between the experimental data at $x = 3.75h$ and the LES data at $x = 5h$, as shown in Fig. 23. The experimental and LES results are very comparable, which is the further evidence of the reliability of the present LES. Increases in the peak frequency as well as the concentration of the PSD at $x = 2.5h$ are also evident in the 2Ds case, but the increase in the concentration of the PSD vanishes in the 2Dr case, indicating high mixing effects in the wake. At $x = 5.0h$, the S_u profiles of the 3Ds, 3Dr, and 2Ds cases are not significantly different from those at $x = 2.5h$, implying that the generated coherent turbulence structure could be transported to the far wake region. Later in this report, the flow structures will be illustrated by using Q-criteria, from which the coherent turbulence structures in the wakes of the 3Ds, 3Dr, and 2Ds configurations can be clearly identified.

Here, for the PSD of the wind velocity, it can be concluded that not only the ground roughness but also the topography will have a considerable influence. More importantly, different locations will yield different velocity PSDs even in the upstream regions of the topographies.

Lu_x was calculated at $x = -2.5h$, $x = 0h$, $x = 2.5h$, and $x = 5h$, and the results are shown in Fig. 24. At $x = -2.5h$, the 3D hill cases show larger Lu_x than the 2D ridge cases. However, for the 2D ridge cases, Lu_x is roughly same as it is above the flat ground. Above the summits of the topographies, Lu_x still exhibits the trend $Lu_x(\text{3Ds}) > Lu_x(\text{3Dr}) > Lu_x(\text{2Ds}) > Lu_x(\text{2Dr})$, but the value of Lu_x is generally greater than it is at $x = -2.5h$. In addition, it is meaningful to note that, in the 3Ds case, Lu_x at $x = 0$, $h' = h$, is almost three times as large as that over smooth flat ground. Downstream from the summit, $x = 2.5h$ and $x = 5h$, Lu_x is quite small below h but increases quickly above h. At $2.5h$, Lu_x converges to its value at about $3h$ in each case and at all x values. In guidelines such as ESDU [79–81], DS 472 [82], IEC [6,74], the length scale is always considered to be a function of only the height and ground roughness in the wind speed calculations. The shape of the topography is rarely taken into consideration. However, the results of our simulation indicate that the effect of the shape of the topography could be very large.

4.4. E and Q

In this section, the mean E and instantaneous Q on the *x*-*z* plane, as well as the Q iso-surface will be shown to make the presentation of the LES data in this study more intuitive.

The time-averaged enstrophy, E_{avg}, is shown in Fig. 25. In the smooth cases (3Ds and 2Ds), the rotation of the fluid is concentrated near the ground due to the shear stress from the non-slip boundary condition. However, the rotation becomes very weak in the rough cases (3Dr and 2Dr), because the drag effects from the vegetation canopy decelerate the wind near the ground, resulting in a moderate velocity gradient and shear stresses. Just after the summits of the topographies, the fluid with strong rotation near the ground in the smooth cases is transported directly to the downstream wake region. Downstream from the summit, the generated and transported vortices grow with increasing distance. The sizes of the vortices increase, and consequently the rotation is slowed

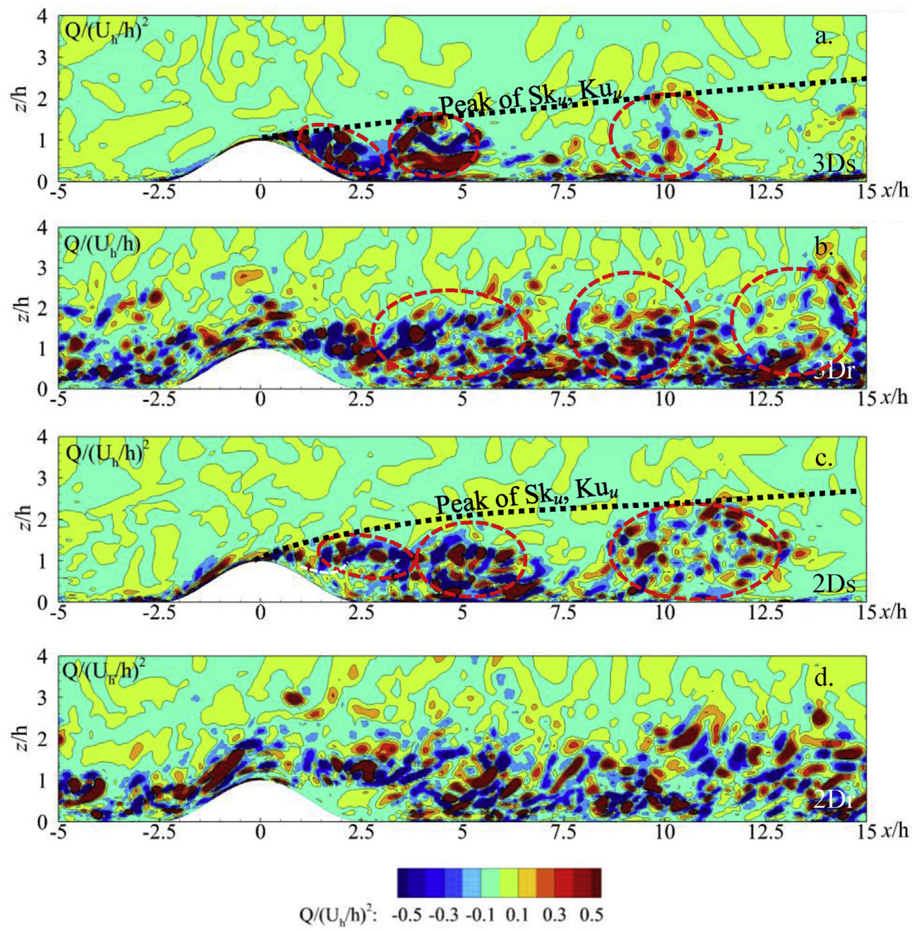

Fig. 26. Distributions of instantaneous Q values on *x-z* plane. (a) 3Ds, (b) 3Dr, (c) 2Ds and (d) 2Dr. Q has been normalized by U_h^2/h^2. *x* and *z* axis have been normalized by h. Thick red dashed lines are the indications of the coherent turbulence structure. Black dashed lines are the indications of the locations of the peak Sk_u and Ku_u. (For interpretation of the references to color in this figure legend, the reader is referred to the Web version of this article.)

down. Therefore, E_{avg} becomes small, but the relatively high E_{avg} regions are large.

The instantaneous Q values are shown in Fig. 26, where the red dashed lines represent the coherent large vortices generated by the topographies. The coherent turbulence structure is much clearer in the smooth cases than in the rough cases. The clear sinusoidal shapes of the vortices in the wakes of the smooth topographies should also be the reason for the skewness and kurtosis concentration. The black dashed lines indicate the locations of the Sk_u and Ku_u peaks. These lines are located at the crests of upper boundaries of the sinusoidal vortex concentrations. Therefore, it can be understood that the fluids periodically experience turbulence structures of two different types at the black dashed lines. One type originates from the background turbulence, and the other type is from the coherent turbulence generated by the topographies. Consequently, the velocity time histories at the black solid dashed lines seem like white noise with large periodic impulses. However, the duration of the impulses is short. Therefore, the kurtosis at the black dashed lines is high. Based on the instantaneous distribution of streamwise velocity (not shown in this paper), we know that the streamwise velocity increases at the crests of the sinusoidal vortex concentration curves. Therefore, the probability of high wind speed is high at the black dashed lines, due to negative skewness. In the rough cases, there is a clear horizontal boundary between the background turbulence and the topography-generated turbulence. Consequently, there is rarely a large impulse in the time history of the streamwise velocity in the wake. That is the reason for the almost 0 skewness and 3.0 kurtosis in the wake of a rough hill or ridge.

Fig. 27 shows snapshots of the instantaneous flow fields visualized by using the iso-surfaces of the Q values. The thick yellow dashed lines indicate the ranges of the hills or ridges, while the thin yellow lines are the central lines of the ridges. Three large vortices could be identified in the wake of the smooth 3D hills and are encircled by green dashed lines (Fig. 27(a and b)). The animation of the fluids revealed that the large vortices in the wake were not randomly generated, but rather had a certain frequency, just like the Karman vortex region downstream from a cylinder. Clear turbulence structure is evident in the 2Ds case (Fig. 27(c)). In this case, the turbulence structure is actually not 2D, but rather has obvious 3D vortex cores, which are identified by green dashed lines and are curved not only in the vertical direction, but also in the horizontal directions. Therefore, it can be concluded that, when modeling the flow fields over topographies, a 3D numerical model is necessary to capture the 3D flow fields in the wake, even if the topography is 2D. However, if vegetation is introduced onto the smooth 2D ridge, the clear 3D turbulence flow fields will be disturbed by the additional turbulence from the vegetation, as shown in Fig. 27(d), where the flow fields become nearly 2D. For the flow fields downstream from the rough 3D hill (Fig. 27(b)), large periodic vortices are still observable, but they have been highly mixed due to the vegetation-generated turbulence.

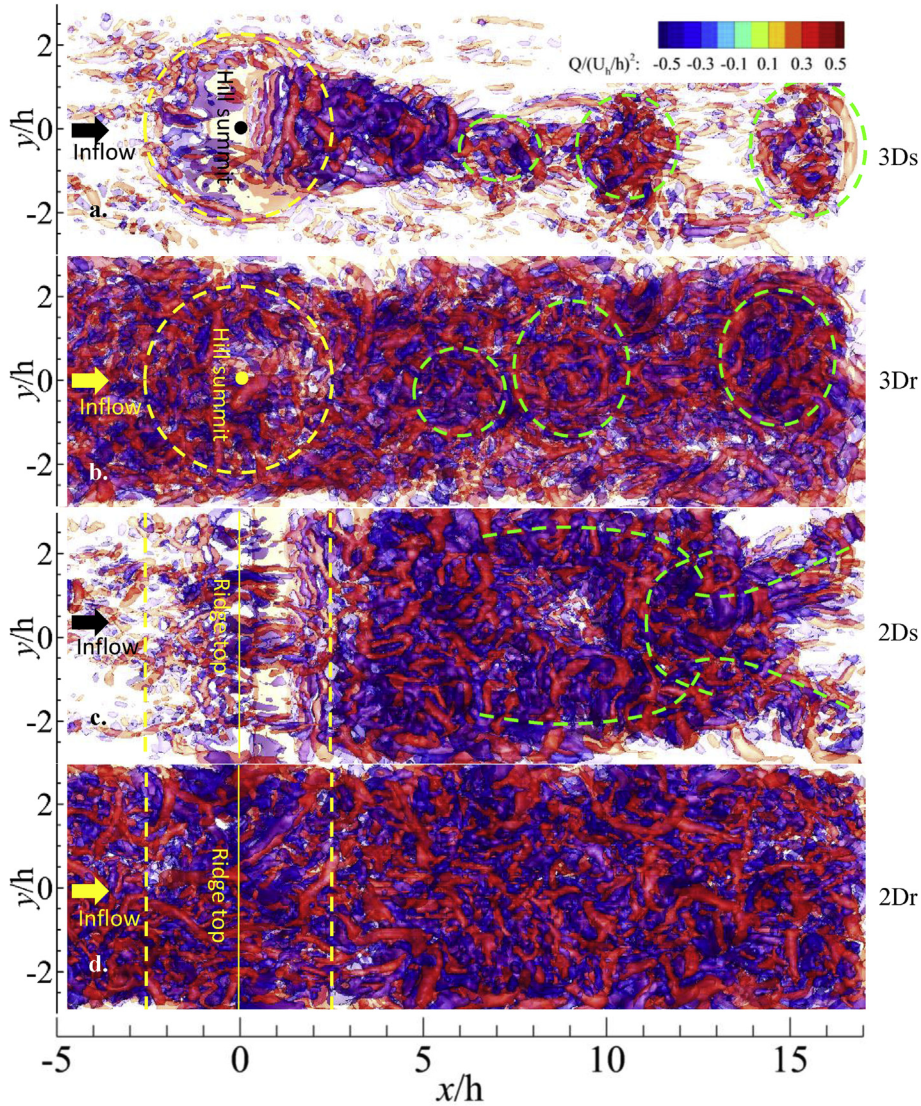

Fig. 27. Bird view of instantaneous iso-surfaces of Q values with positive being red and negative being blue. (a) 3Ds, (b) 3Dr, (c) 2Ds and (d) 2Dr. Q has been normalized by U_h^2/h^2. x and z axis have been normalized by h. Yellow solid lines indicate the center of the ridges and the yellow dashed lines show the range covered by the topographies. Green dashed lines illustrate the coherent turbulent structures in the wake. (For interpretation of the references to color in this figure legend, the reader is referred to the Web version of this article.)

5. Conclusions

In the present study, LESs were conducted to reproduce the turbulent flow fields over 3D hills and 2D ridges with different roughness conditions on the ground. Four simplified topographies, i.e., a 3D hill with smooth ground, a 3D hill with rough ground, a 2D ridge with smooth ground, and a 2D ridge with rough ground, were examined. The means and fluctuations of the velocities that were determined using the present LES were compared with those obtained experimentally, and the values of R_{uu}, Sk_u, Ku_u, S_u, and Lu_x of the streamwise velocity were examined. These parameters are important for both determining 3D flow fields using analytical methods and calculating the fatigue loads of wind turbines. Finally, the coherent turbulent flow fields were visualized by using E and Q. The conclusions and findings of this study can be summarized as follows.

1. The comparison of U_i, u_i, and the recirculation bubble shapes with those obtained experimentally demonstrate that the LES could predict the turbulent flow fields over the topographies well.
2. R_{uu} covered larger areas in the smooth cases than in the rough cases. In addition, changing the shape of the topography from a 3D hill to a 2D ridge caused R_{uu} to decrease considerably. Furthermore, in each case and at all of the locations, R_{uu} covered a larger area in the streamwise direction than in the vertical and spanwise directions. This finding indicates that R_{uu} is a function not only of the distance to the reference point, but also the ground roughness, location, topography shape, and direction.
3. When determining the wind-induced fatigue loads of wind turbines, the widely used Weibull distribution of the PDF should be adopted with caution, especially for the shear layer region in which large kurtosis and negative skewness occur.
4. There was an obvious concentration of PSD in the wake in the 3Ds, 3Dr, and 2Ds cases, indicating the existence of coherent turbulence structures. More importantly, different locations yielded different velocity PSDs even in the upstream regions of the topographies. Furthermore, there was a significant jump in

the turbulence length scale just above the summit of the smooth 3D hill.

5. A Karman vortex region downstream from the 3D hills could be identified. It is interesting that the turbulence structure in the wake for the smooth 2D ridge was actually not 2D, but rather had obvious 3D vortex cores. When vegetation was introduced on the ground of the 2D ridge, the clear 3D turbulence flow fields were disturbed.

The present study is limited in that the topography was simplified as isolated 3D hills or 2D ridges. Further study should be conducted in the future to considering the actual topographies.

Acknowledgement

Supports from the National Key Research and Development Plan of China (2016YFE0127900, 2016YFC0800206), the National Natural Science Foundations of China (51608220), the Project of Innovation-driven Plan in Huazhong University of Science and Technology (2017KFYXJJ141), are gratefully acknowledged.

References

[1] Z. Şen, Terrain topography classification for wind energy generation, Renew. Energy 16 (16) (1999) 904–907.
[2] M. Bilal, Y. Birkelund, M. Homola, S. Virk, A. Kalogirou, P. Christodoulides, Wind over complex terrain - microscale modelling with two types of mesoscale winds at Nygårdsfjell, Renew. Energy 99 (2016) 647–653.
[3] H. Kim, C. Lim, Effect of island topography and surface roughness on the estimation of annual energy production of offshore wind farms, Renew. Energy 103 (2017) 106–114.
[4] Z. Dhunny, R. Lollchund, V. Rughooputh, Wind energy evaluation for a highly complex terrain using computational fluid dynamics (CFD), Renew. Energy 101 (2017) 1–9.
[5] D. Argüeso, S. Businger, Wind power characteristics of Oahu, Hawaii, Renew. Energy 128 (2018) 324–336.
[6] IEC, Wind Turbines – Part 1: Design Requirements, International Standard, third ed., International Electrotechnical Commission, 2005, pp. 61400–61401.
[7] N. Dimitrov, A. Natarajan, M. Kelly, Model of wind shear conditional on turbulence and its impact on wind turbine loads, Wind Energy 18 (11) (2015) 1917–1931.
[8] A.B. Tabrizi, J. Whale, T. Lyons, T. Urmee, J. Peinke, Modelling the structural loading of a small wind turbine at a highly turbulent site via modifications to the Kaimal turbulence spectra, Renew. Energy 105 (2017) 288–300.
[9] A. Theodorakakos, G. Bergeles, A telescopic local grid refinement technique for wind flow simulation over complex terrain, Wind Energy 4 (2) (2010) 77–98.
[10] K. Røkenes, Å. Krogstad, Wind tunnel simulation of terrain effects on wind farm siting, Wind Energy 12 (4) (2009) 391–410.
[11] A. Kasmi, C. Masson, Turbulence modeling of atmospheric boundary layer flow over complex terrain: a comparison of models at wind tunnel and full scale, Wind Energy 13 (8) (2010) 689–704.
[12] A. Bechmann, N. Sørensen, Hybrid RANS/LES method for wind flow over complex terrain, Wind Energy 13 (1) (2010) 36–50.
[13] A. Bechmann, N. Sørensen, Hybrid RANS/LES applied to complex terrain, Wind Energy 14 (2) (2011) 225–237.
[14] A. Cuerva-Tejero, S. Avila-Sánchez, J. Pérez-Alvarez, S. Yeow, Measurement of spectra over the bolund hill in wind tunnel, Wind Energy 21 (2) (2018).
[15] G. Kim, M. Lee, C. Lim, H. Kyongb, An experimental and numerical study on the flow over two-dimensional hills, J. Wind Eng. Ind. Aerod. 66 (1997) 17–33.
[16] P. Carpenter, N. Locke, Investigation of wind speeds over multiple two-dimensional hills, J. Wind Eng. Ind. Aerod. 83 (1999) 109–120.
[17] A. Ferreira, A. Lopes, D. Viegas, A. Sousa, Experimental and numerical simulation of flow around two-dimensional hills, J. Wind Eng. Ind. Aerod. 54 (55) (1995) 173–181.
[18] S. Cao, T. Wang, Y. Ge, Y. Tamura, Numerical study on turbulent boundary layers over two-dimensional hills-Effects of surface roughness and slope, J. Wind Eng. Ind. Aerod. 104 (106) (2012) 342–349.
[19] T. Takahashi, T. Ohtsu, F. Yassin, S. Kato, S. Murakami, Turbulence characteristics of wind over a hill with a rough surface, J. Wind Eng. Ind. Aerod. 90 (2002) 1697–1706.
[20] S. Cao, T. Tamura, Effects of roughness blocks on atmospheric boundary layer flow over a two-dimensional low hill with/without sudden roughness change, J. Wind Eng. Ind. Aerod. 95 (2007) 679–695.
[21] D. Poggi, G. Katul, The effect of canopy roughness density on the constitutive components of the dispersive stresses, Exp. Fluid 45 (2008) 111–121.
[22] T. Banerjee, G. Katul, S. Fontan, D. Poggi, M. Kumar, Mean flow near edges and within cavities situated inside dense canopies, Boundary-Layer Meteorol. 149 (2013) 19–41.
[23] X. Xu, C. Yi, E. Kutter, Stably stratified canopy flow in complex terrain, Atmos. Chem. Phys. 15 (2015) 7457–7470.
[24] D. Lubitz, R. White, Wind-tunnel and field investigation of the effect of local wind direction on speed-up over hills, J. Wind Eng. Ind. Aerod. 95 (2007) 639–661.
[25] Z. Liu, T. Ishihara, T. Tanaka, X. He, LES study of turbulent flow fields over a smooth 3D hill and a smooth 2-D ridge, J. Wind Eng. Ind. Aerod. 153 (2016a) 1–12.
[26] W. Gong, A. Ibbetson, A wind tunnel study of turbulent flow over model hills, Boundary-Layer Meteorol. 49 (1989) 113–148.
[27] J.J. Finnigan, R. Raupach, E.F. Bradley, G.K. Aldis, A wind tunnel study of turbulent flow over a two-dimensional ridge, Boundary-Layer Meteorol. 50 (1990) 277–317.
[28] E. Neff, N. Meroney, Wind-tunnel modeling of hill and vegetation influence on wind power availability, J. Wind Eng. Ind. Aerod. 74–76 (1998), 35-343.
[29] T. Ishihara, S. Oikawa, K. Hibi, Wind tunnel study of turbulent flow over a three-dimensional steep hill, J. Wind Eng. Ind. Aerod. 83 (1999) 95–107.
[30] S. Cao, T. Tamura, Experimental study on roughness effects on turbulent boundary layer flow over a two-dimensional steep hill, J. Wind Eng. Ind. Aerod. 94 (2006) 1–19.
[31] H. Kobayashi, F. Pereira, M.B.B. Siqueira, Numerical study of the turbulent flow over and in a model forest on a 2D hill, J. Wind Eng. Ind. Aerod. 53 (1994) 357–374.
[32] T. Utnes, J. Eidsvik, Turbulent flows over mountainous terrain modelled by the Reynolds equations, Boundary-Layer Meteorol. 79 (1996) 393–416.
[33] J. Kim, J. Baik, Y. Chunb, Two-dimensional numerical modeling of flow and dispersion in the presence of hill and buildings, J. Wind Eng. Ind. Aerod. 89 (2001) 947–966.
[34] T. Ishihara, K. Hibi, Numerical study of turbulent wake flow behind a three-dimensional steep hill, Wind Struct. Int. J. 5 (2002) 317–328.
[35] S. Iizuka, H. Kondo, Performance of various sub-grid scale models in large-eddy simulations of turbulent flow over complex terrain, Atmos. Environ. 38 (2004) 7083–7091.
[36] S. Iizuka, H. Kondo, Large-eddy simulations of turbulent flow over complex terrain using modified static eddy viscosity models, Atmos. Environ. 40 (2006) 925–935.
[37] R. Loureiro, A.T.P. Alho, S. Freire, The numerical computation of near-wall turbulent flow over a steep hill, J. Wind Eng. Ind. Aerod. 96 (2008) 540–561.
[38] B. Mello, I. Yanagihara, Numerical prediction of gas concentrations and fluctuations above a triangular hill within a turbulent boundary layer, J. Wind Eng. Ind. Aerod. 98 (2010) 113–119.
[39] D. Griffiths, H. Middleton, Simulations of separated flow over two-dimensional hills, J. Wind Eng. Ind. Aerod. 98 (2010) 155–160.
[40] F. Wan, F. Porté-Agel, Large-eddy simulation of stably-stratified flow over a steep hill, Boundary-Layer Meteorol. 138 (2011) 367–384.
[41] M. Diebold, C. Higgins, J. Fang, A. Bechmann, M.B. Parlange, Flow over hills: a large-eddy simulation of the bolund case, Boundary-Layer Meteorol. 148 (2013) 177–194.
[42] Z. Liu, T. Ishihara, X. He, H. Niu, LES study on the turbulent flow fields over complex terrain covered by vegetation canopy, J. Wind Eng. Ind. Aerod. 155 (2016b) 60–73.
[43] Y. Ma, H. Liu, Large-eddy simulations of atmospheric flows over complex terrain using the immersed-boundary method in the weather research and forecasting model, Boundary-Layer Meteorol. 165 (2017) 421–445.
[44] Y. Chang, J. Schmidt, M. Dörenkämper, B. Stoevesandt, A consistent steady state CFD simulation method for stratified atmospheric boundary layer flows, J. Wind Eng. Ind. Aerod. 172 (2018) 55–67.
[45] T. Takahashi, S. Kato, S. Murakami, R. Ooka, Y.M. Fassy, R. Kono, Wind tunnel tests of effects of atmospheric stability on turbulent flow over a three-dimensional hill, J. Wind Eng. Ind. Aerod. 93 (2005) 155–169.
[46] S.G. Sajjadi, T.J. Craft, Y. Feng, A numerical study of turbulent flow over a two-dimensional hill, Int. J. Numer. Methods Fluid. 35 (1) (2015) 1–23.
[47] L. Yu, A. Mochida, S. Murakami, H. Yoshino, T. Shirasawa, Numerical simulation of flow over topographic features by revised k-ε models, J. Wind Eng. Ind. Aerod. 91 (1–2) (2003) 231–245.
[48] T. Tamura, S. Cao, A. Okuno, LES study of turbulent boundary layer over a smooth and a rough 2D hill model, Flow, Turbul. Combust. 79 (2007a) 405–432.
[49] T. Tamura, A. Okuno, Y. Sugio, LES analysis of turbulent boundary layer over 3D steep hill covered with vegetation, J. Wind Eng. Ind. Aerod. 95 (2007b), 1463-147.
[50] Z. Liu, S. Cao, H. Liu, T. Ishihara, Large-Eddy Simulations of the Flow over an Isolated Three-Dimensional Hill, Boundary-Layer Meteorol, 2018, pp. 1–27.
[51] J. Smagorinsky, General circulation experiments with the primitive equations, Mon. Weather Rev. 91 (1963) 99–164.
[52] K. Lilly, A proposed modification of the Germano subgrid-scale closure model, Phys. Fluids A 4 (1992) 633–635.
[53] H. Ferziger, M. Peric, Computational Method for Fluid Dynamics, third ed., Springer, Berlin, 2002.
[54] S. Dupont, Y. Brunet, Edge flow and canopy structure: a large-eddy simulation study, Boundary-Layer Meteorol. 126 (2008) 51–71.
[55] J. Mason, J. Thomson, Large-eddy simulations of the neutral-static-stability planetary boundary layer, Q. J. R. Meteorol. Soc. 113 (1987) 413–443.
[56] R. Courant, K. Friedrichs, H. Lewy, Über die partiellen differenzengleichungen

der mathematischen physik, Math. Ann. 100 (1928) 32–74 (in German).
[57] Ansys Inc, Ansys Fluent 14.0 User's Guide, 2014 (U.S).
[58] T. Ishihara, K. Hibi, An experimental study of turbulent boundary layer over steep hills, in: Proc of the 15th National Symposium on Wind Engineering, 1998, pp. 61–66 (in Japanese).
[59] C. Kaimal, J. Finnigan, Atmospheric Boundary Layer Flows, Oxford University Press, Oxford, UK, 1994.
[60] T. Ishihara, Measurements and predictions of local wind field in complex terrain, J. Wind Eng. 89 (2001) 245–248.
[61] L. Ding, L. Street, Numerical study of the wake structure behind a three-dimensional hill, J. Atmos. Sci. 60 (2003) 1678–1690.
[62] B. Conan, A. Chaudhari, S. Aubrun, V. Beeck, J. Hämäläinen, A. Hellsten, Experimental and numerical modelling of flow over complex terrain: the bolund hill, Boundary-Layer Meteorol. 158 (2016) 183–208.
[63] S. Khani, F. Porté-Agel, A modulated-gradient parametrization for the large-eddy simulation of the atmospheric boundary layer using the weather research and forecasting model, Boundary-Layer Meteorol. 165 (2017) 385–404.
[64] R. DeLeon, M. Sandusky, I. Senocak, Simulations of turbulent flow over complex terrain using an immersed-boundary method, Boundary-Layer Meteorol. (2018) 1–22.
[65] B. Goger, M. Rotach, A. Gohm, O. Fuhrer, I. Stiperski, A. Holtslag, The impact of three-dimensional effects on the simulation of turbulence kinetic energy in a Major Alpine Valley, Boundary-Layer Meteorol. (2018) 1–27.
[66] J. Hunt, W. Snyder, Experiments on stably and neutrally stratified flow over a model three-dimensional hill, J. Fluid Mech. 96 (4) (1980) 671–704.
[67] M. Garcíavillalba, N. Li, W. Rodi, M. Leschziner, Large-eddy simulation of separated flow over a three-dimensional axisymmetric hill, J. Fluid Mech. 627 (627) (2009) 55–96.
[68] H. Shaw, Y. Brunet, J. Finnigan, R. Raupach, A wind tunnel study of air flow in waving wheat: two-point velocity statistics, Boundary-Layer Meteorol. 76 (1995) 349–376.
[69] R. Raupach, A. Antonia, S. Rajagopalan, Rough-wall turbulent boundary layers, Appl. Mech. Rev. 44 (1991) 1–25.
[70] B. Su, H. Shaw, T. Paw, Two-point correlation analysis of neutrally stratified flow within and above a forest from large-eddy simulation, Boundary-Layer Meteorol. 94 (2000) 423–460.
[71] D. Childers, Modern Spectrum Analysis, IEEE Press, New York, 1978. Chapter II.
[72] S. Kay, S. Marple, Spectrum analysis: a modern perspective, Proc. IEEE 69 (1981) 1380–1419.
[73] W. Press, S. Teukolsky, W. Vetterling, B. Flanney, Numerical recipes, in: The Art of Scientific Computing, third ed., Cambridge University Press, 2007, pp. 681–685.
[74] IEC, Wind Turbine Generator Systems – Part 1: Safety Requirements, International Standard 61400–1 Edition 2, International Electrotechnical Commission, 1999.
[75] A. Celik, A statistical analysis of wind power density based on the Weibull and Rayleigh models at the southern region of Turkey, Renew. Energy 29 (4) (2004) 593–604.
[76] J. Wallace, L. Ong, P. Moin, The Velocity and Vorticity Fields of the Turbulent Near Wake of a Circular Cylinder, National Aeronautics and Space Administration Report, 1995.
[77] K. Lee, K. Chang, Re-evaluating wake width in turbulent shear flow behind an axisymmetric cylinder by means of higher order turbulence statistics, J. Fluid Sci. Technol. 9 (3) (2014) 1–6.
[78] A. Kolmogorov, The local structure of turbulence in incompressible viscous fluid for very large Reynolds numbers, Proc. USSR Acad. Sci. 30 (1941) 299–303 (in Russian).
[79] ESDU, Characteristics of Atmospheric Turbulence Near the Ground. Part III: Variations in Space and Time for Strong Winds (Neutral Atmosphere), ESDU 75001, Engineering Sciences Data Unit, London, 1975.
[80] ESDU, Strong Winds in the Atmospheric Boundary Layer. Part 2: Discrete Gust Speeds, ESDU 83045, Engineering Sciences Data Unit, London, 1983.
[81] ESDU, Characteristics of Atmospheric Turbulence Near the Ground. Part II: Single Point Data for Strong Winds (Neutral Atmosphere), Engineering Sciences Data Unit, London, 1985.
[82] DS 472, Code of Practice for Loads and Safety of Wind Turbine Constructions, DS 472, The Danish Society of Engineers and the Federation of Engineers, 1992.